# Highlights

**Low-cost real-time monitoring and automated control system for a bench-scale portable downdraft gasifier**

Antonio Rodríguez Orta, Manuel Sánchez Raya, Roque Aguado Molina, Juan Antonio Gómez Galán, David Vera Candeas, Diego A. López García

- A low-cost system is developed with OTA updates and an intuitive interface.
- Various biomass types can be characterized using minimal raw material.
- The monitoring system is designed for easy operation and low maintenance.
- Target temperature is reached and stabilized within 20–25 minutes from room temperature.
- The system is stabilized through user adjustments within 10 minutes after steady state.

# Low-cost real-time monitoring and automated control system for a bench-scale portable downdraft gasifier

Antonio Rodríguez Orta[a], Manuel Sánchez Raya[a], Roque Aguado Molina[b], Juan Antonio Gómez Galán[a,*], David Vera Candeas[b], Diego A. López García[a]

[a]*Departamento de Ingeniería Electrónica, Sistemas Informáticos y Automática, Escuela Técnica Superior de Ingeniería, Universidad de Huelva, Avda. de las Fuerzas Armadas s/n, 21007 Huelva, Spain*
[b]*Departamento de Ingeniería Eléctrica, Escuela Politécnica Superior de Linares, Universidad de Jaén, Avda. de la Universidad s/n, 23700 Linares, Spain*

**Abstract**

This research work focuses on the development of a real-time monitoring and automated control system for a portable biomass gasification prototype to generate electricity from agricultural waste. The prototype consists of an air-blown downdraft fixed-bed gasifier and a producer gas conditioning unit, which operate together in a remotely controlled ensemble. This system not only facilitates the collection and storage of operational data, but also allows temperature settings to be adjusted to accommodate diverse biomass types, enabling real-time monitoring and control of system performance from any location. The proposed system stands out for its simple and low-cost design, making it suitable for implementation in small agricultural facilities, especially in remote and off-grid areas where conventional electrification is limited or non-existent. Moreover, its compact size, transportability, and low fuel consumption make it a valuable research tool for testing the gasification performance with diverse biomass types, thus facilitating the determination of key parameters in the design of larger-scale gasification plants. This study presents the results of two preliminary tests aimed at assessing the performance of the monitoring system. The findings reveal that the gasifier can reach the target temperature in less than 25 minutes, depending on the test conditions. This is made possible by the implemented temperature control system, which allows the gasifier to maintain the target temperature for extended periods with controlled oscillations. The system's graphical interface enables intuitive, real-time, and remote monitoring and management of temperatures in several zones along the gasifier's height. Additionally, the interface allows manual or algorithmic control of the system's actuators, with the ability to modify the control algorithms through over-the-air updates.

*Keywords:* Biomass gasification, Producer gas, Process automation, Real-time system, Remote access, Low power consumption

*Corresponding author

*Email addresses:* antonio.rodriguez@diesia.uhu.es (Antonio Rodríguez Orta), msraya@diesia.uhu.es (Manuel Sánchez Raya), ramolina@ujaen.es (Roque Aguado Molina), jgalan@diesia.uhu.es (Juan Antonio Gómez Galán), dvera@ujaen.es (David Vera Candeas), diego.lopez@diesia.uhu.es (Diego A. López García)

## 1. Introduction

The agrifood industry is a significant contributor to global waste production, with large amounts of biomass generated during agricultural and food processing activities. If properly managed, agroindustrial waste holds significant potential to become a valuable resource for energy recovery, especially in remote locations with abundant biomass resources. Through the process of gasification, agroindustrial waste can be used for decentralized renewable electricity generation [1]. This thermochemical conversion process involves subjecting a solid carbonaceous feedstock to partial oxidation with a gasifying agent, typically air, oxygen, and/or steam [2]. For small-scale gasification systems designed for electricity generation, air is usually the preferred option due to its economic advantages [3–5]. The gasification process using air as gasifying agent allows the conversion of organic carbon materials, such as agroindustrial biomass waste, into a lean fuel gas suitable for power generation known as producer gas [6, 7].

Gasifiers are broadly classified as fixed bed, fluidized bed, and entrained flow [2]. Fixed-bed gasifiers are in turn subcategorized into updraft, downdraft, and crossdraft types. Downdraft gasifiers are characterized by a parallel downward flow of both the solid feedstock and the gasifying agent. In this design, the gasifying agent (i.e., air) is introduced below the upper area and the producer gas is extracted through the lower part of the reactor. Downdraft gasifiers are the preferred option for small-scale distributed power generation due to their simple construction, reliable operation, short startup time (20–30 minutes), adaptability to various biomass feedstocks, and high carbon conversion efficiency [2, 5, 8, 9]. As a result of these advantages, downdraft gasifiers currently dominate the market, especially in power generation applications, accounting for roughly three-fourths of all gasifiers marketed commercially [10]. Additionally, they produce less tar because the oxidation zone immediately follows the pyrolysis zone, where these compounds are formed [2]. This characteristic makes downdraft gasifiers particularly suitable for small-scale electricity production with internal combustion engines (ICEs), especially for applications requiring up to 1 MW of thermal power [2]. However, the producer gas must be cooled before use

as a result of the high reactor outlet temperature [11]. Small-scale downdraft gasifiers provide the added advantage of being containerizable for convenient transportation and can even be designed as mobile power generation units [9]. As main drawbacks, downdraft gasifiers generally exhibit lower thermal performance compared to other technologies and may face challenges when processing biomass feedstocks with high ash and moisture content. Downdraft gasifiers can be subclassified into two major design variants: throated (also known as constricted) and throatless (also known as topless, open top, or open core). Constriction in the combustion stage favors the thermal cracking of most of the tar by forcing all pyrolysis products to pass through a narrow section, thus improving the quality of the producer gas [2, 12, 13].

The gasification process can be divided into four main stages: drying or dehydration, pyrolysis or volatilization, combustion or oxidation, and gasification or reduction [2, 14, 15]. In fixed-bed gasifiers, these reactions occur in specific areas, whereas, in fluidized-bed gasifiers, the reactions can occur simultaneously throughout the reactor. However, during the actual operation, the four reaction zones commonly overlap with no clear or discrete separation between them [14]. In the drying stage, the solid fuel reaches temperatures up to 200 °C, losing most of its moisture and reducing its content to around 5% [16]. Pyrolysis follows, where biomass chemical bonds break (thermolysis) at temperatures in the range of 150 to 700 °C, leading to pyrolytic products (including both light and heavy hydrocarbons, the latter commonly known as tars) [2, 15, 17]. Drying and volatilization occur simultaneously, producing gaseous, liquid, and solid fractions. Non-condensable gases make up 70% to 90% by weight of the products [17]. In the combustion zone, temperatures reach between 500 and 1500 °C due to exothermic oxidation of pyrolysis products in oxygen's presence [18, 19]. Oxidation must occur with limited oxygen to avoid complete fuel combustion [17]. Heat from combustion drives drying, pyrolysis, and gasification. Using air as a gasifying agent introduces inert gases like nitrogen ($N_2$) and argon (Ar) into the product gas [17]. Finally, in the gasification zone, hydrogen ($H_2$), carbon monoxide (CO), and methane ($CH_4$) are formed through reduction reactions of oxidized carbonaceous solids with downstream gases.

This endothermic process occurs at temperatures in the range of 600 to 1100 °C [2, 17, 18]. As temperature changes affect gas composition and tar concentration, strict control over the process temperature is essential. Higher temperatures increase carbon conversion and reduce tar formation, but also lead to an increased risk of ash sintering and a decline in the calorific value of the product gas [17].

Automation and control systems for biomass gasifiers have advanced significantly in recent years. Early automation systems relied on basic functionalities such as temperature monitoring or implementing proportional-integral-derivative (PID) controllers for specific process variables, which proved inadequate for dynamic biomass conditions. Sagüés et al. [20] introduced a fuzzy inference system (FIS) to control gasifiers, encoding expert knowledge into if-then rules. This approach allowed the system to dynamically adjust process parameters like air flow and grate frequency based on biomass type and moisture content, enhancing adaptability and process efficiency. Gandhi et al. [21] developed a fuzzy logic controller (FLC) for downdraft gasifiers, utilizing a multi-input multi-output (MIMO) system to regulate temperature and $CO/CO_2$ ratio. Their approach significantly improved stability and response time compared to conventional PID controllers, demonstrating the effectiveness of FLC in handling the nonlinear dynamics of biomass gasification. Gøbel et al. [22] advanced the field with a dynamic one-dimensional mathematical model that incorporated conservation laws and reaction kinetics to optimize stationary performance and identify efficient control strategies for handling load changes. Striūgas et al. [23] further demonstrated practical advancements in automation by integrating staged air supplies, moving grates, and pressure-based char discharge systems into multi-fuel downdraft gasifiers. Their work highlighted the importance of controlling parameters such as bed pressure and temperature to enable effective gasification of diverse biomass feedstocks. More recently, Daniel and Gandhi [24] focused on improving PID controller performance for downdraft gasifiers by utilizing particle swarm optimization (PSO) and adaptive neuro-fuzzy inference system (ANFIS) techniques. Their work demonstrated that PSO and ANFIS-based PID tuning outperformed traditional

Ziegler-Nichols methods in temperature control, providing better transient response and reduced overshoot.

Despite the aforementioned improvements in the control and optimization of biomass gasifiers, there are still numerous opportunities for further research. A remarkable gap in the relevant scientific literature is the development of more intuitive, low-maintenance monitoring and automated control systems that are suitable for portable biomass gasifiers in remote locations. Many existing systems tend to be complex and require skilled personnel for maintenance, which limits their applicability in off-grid settings where simplicity and reliability are crucial. Accordingly, this paper presents an intuitive, low-maintenance monitoring system for a compact, portable biomass gasifier intended for electric power generation in remote locations. The system is specifically designed for transportability and ease of maintenance. Additionally, the compact control unit (housed in a $250 \times 250 \times 100$ mm waterproof enclosure) enhances portability, enabling quick installation and flexible deployment in diverse environments. The proposed system not only collects and stores operational data, but also provides real-time monitoring and remote control capabilities, enabling adjustments to working temperatures to accommodate different biomass types. These features make the system highly adaptable and user-friendly, addressing a gap in the market for easy-to-operate biomass gasifiers that can drive electrification in remote or underserved areas.

## 2. Methodology

This section outlines the rationale behind the selected design, focusing on simplicity, cost-effectiveness, and ease of use. The monitoring and automated control system features compact, high-precision hardware utilizing low-cost commercial sensors and actuators. Additionally, an intuitive graphical interface allows for straightforward remote management, enhancing both usability and operational efficiency at physical and software levels.

### 2.1. *Biomass feedstock characterization and choice of gasifying agent*

Biomass gasification processes are inherently complex due to their multivariable, nonlinear behavior, as well as the variability of biomass properties such as chemical composition, moisture content, and particle size. In the experiments presented in this paper, olive pomace pellets were used as feedstock, the physicochemical properties of which can be consulted in a previous work of some of the authors [5]. Air was used as gasifying agent, due to its availability and low cost [4, 5]. As mentioned above, the resulting gaseous product from air-blown gasification is a lean fuel gas with a high content of inert gases known as producer gas. Despite its relatively low calorific value, it is still suitable for power generation using ICEs [7, 25].

### 2.2. *Design of the biomass gasifier*

Among the various available alternatives, a downdraft fixed-bed reactor was selected in this study for the reasons outlined in Section 1. The height of the reactor is 1.4 m, making it easily transportable. This reactor uses gravity as the driving force to move the fuel from the feed hopper (upper section) to the combustion zone (lower section), where the highest temperatures are reached [2]. In this study, a downdraft reactor with a constriction in the combustion zone was used. The inclusion of a constriction zone forces the products from pyrolysis to pass through a narrow passage, where they undergo combustion in a process known as flaming pyrolysis, thereby reducing the formation of tar [2, 15]. Furthermore, temperatures above 800 °C are reached, promoting thermal cracking reactions, which significantly reduce the tar content in the producer gas [26]. This reduction in tar content is critical, not only for improving the quality of the producer gas, but also for lowering the operation and maintenance costs, as tar deposits can lead to clogging and damage to equipment.

The gasification process produces a lean fuel gas known as producer gas, which can be used to power a generator set for electricity generation [7]. Downstream of the reactor, the system includes a series of filtering components to remove byproducts such as tar and water vapor, which can

negatively impact engine performance. Another design consideration is the elevated temperature at which the producer gas is generated, which can be detrimental to the engine–generator set. To mitigate this issue, a heat exchanger is used to reduce the outlet temperature.

A balance between the output power and producer gas yield is achieved through careful temperature control during operation. The temperature within the gasifier is regulated by adjusting the airflow rate. In addition, the design incorporates gas conditioning and filtration elements to ensure continuous operation without frequent maintenance interruptions. These components, including the sensors, actuators, gas filtration equipment, and adaptation components, are schematically illustrated in Fig. 1.

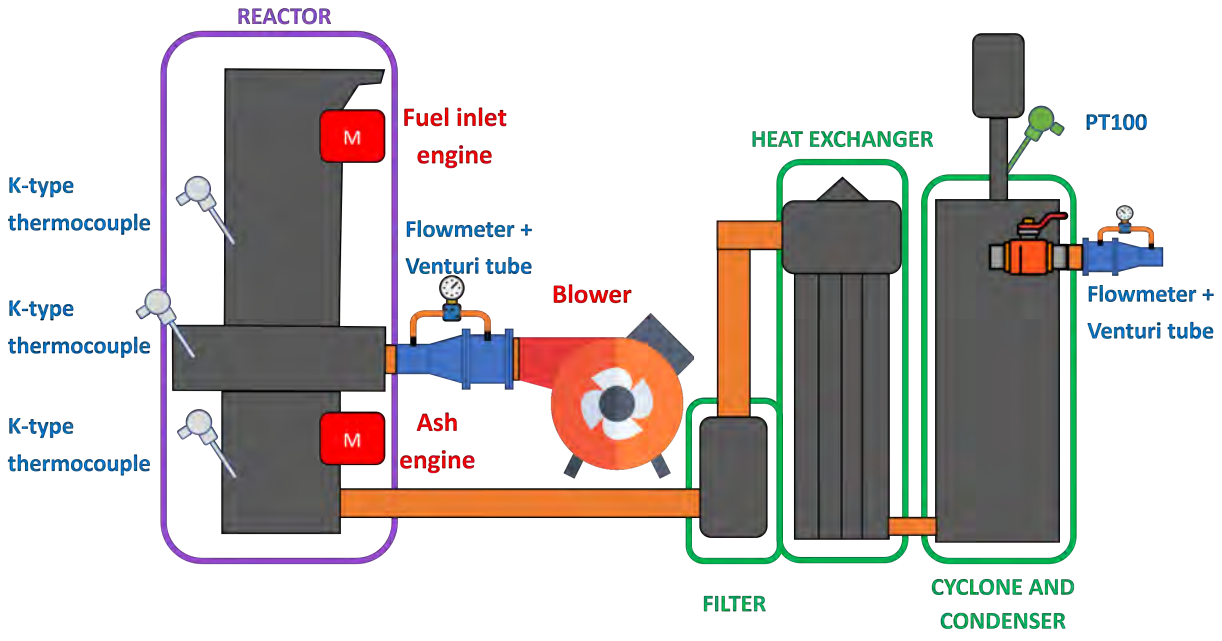


Figure 1: Overview of the prototype assembly, highlighting its main components.

Biomass decomposition under substoichiometric operating conditions generates a dense mist composed of water vapor and tar that adheres to the system walls and is carried downstream by the continuous flow of gas. The producer gas leaves the gasification reactor at around 400 °C [5], and contains particulates, condensates, tar, and water vapor [15]. This hot producer gas must be cooled and cleaned, ensuring it is virtually free from tar, water vapor, and particulates, and at near

ambient temperature if it is to be utilized in an internal combustion engine [15]. In this study, a compact producer gas conditioning system is included to support extended operation with reduced maintenance (see Fig. 1). This system consists of a gas-air countercurrent-flow heat exchanger that lowers exhaust gas temperature from 400 °C to about 50 °C, suitable for the engine–generator set; a cyclone that redirects part of the inlet airflow to the heat exchanger outlet to avoid particle buildup in the condenser; a condenser that traps contaminants at the bottom of a container to prevent them from circulating through the piping; and an ash collection box with a removable door for easy withdrawal of accumulated residues after several hours of operation.

### *2.3. Operating procedure*

The first step is to load the reactor with the biomass feedstock and securely seal it against air leakage [27]. Proper sealing is essential to maintain control over the reactor's internal conditions, as the centrifugal blower is the sole component responsible for injecting a regulated amount of air into the reactor. To ensure that the product gas is usable for power generation applications and contains a minimal number of contaminants, the goal is to achieve a chemical decomposition reaction of organic matter under substoichiometric conditions [2]. Gasification reactions occur at elevated temperatures in an oxygen-lean atmosphere, which reflects the paramount importance of an air-tight sealing [28–30].

After sealing against leakage, combustion must be initiated manually, a process that lasts for approximately 20 min depending on the moisture content of the feedstock [5]. During this stage, a blowtorch provides heat, and the blower injects as much air as possible, thereby promoting heat distribution and the formation of the first layer of charred particles in the combustion chamber. Once the process has become self-sustaining, the user can switch to automatic mode. In this mode, the system automatically regulates the air intake to the reactor by adjusting the airflow rate based on feedback from the temperature sensors integrated into the reactor. The aim of the electronic system is to maintain operation within established temperature ranges, facilitating the gravity-driven movement of the feedstock through the different sections of the reactor, while si-

multaneously eliminating ash deposits from the walls through vibrations generated by two motors placed at the bottom of the reactor.

During the biomass gasification process, it is essential to maintain the temperature in the combustion zone at around 800 °C to provide the required heat supply for the endothermic pyrolysis and reduction reactions, as well as for minimizing tar production [3, 31, 32]. Tar is detrimental to both the environment and the power generation unit, thereby reducing its lifespan [26]. The producer gas from the reactor is at elevated temperatures and may contain impurities, necessitating pretreatment before it can be used in an engine. Filtration removes impurities such as dust, tar, and moisture, which may clog the intake manifold of the engine and increase maintenance requirements. The heat exchanger reduces the gas temperature from approximately 400 °C at the reactor outlet to around 50 °C, making it suitable for engine operation. After the conditioning stage, the system is equipped with a T-valve that allows the producer gas to be routed either to the flare stack or to the generator set. An effective approach to determine whether the producer gas has an adequate calorific value is to ignite it. A blue flame indicates the gas is appropriate for use as fuel [5], thereby avoiding the need for an expensive gas analyzer.

### *2.4. Hardware design*

Temperature and airflow sensors were strategically placed to evaluate the performance of the prototype and determine whether they satisfy the design specifications. These sensors provide real-time data on the state of the system, enabling the implementation of necessary actions to stabilize the pyrolysis reaction. The key parameter for maintaining this reaction is the combustion temperature. The reactor, in conjunction with the control unit, must sustain the temperature at approximately 800 °C, with a narrow allowable range (±25 °C). Temperature stability depends on the volume of air introduced as an oxidizer. The control unit adjusts the control signal using pulse width modulation (PWM) of the blower based on the data provided by the temperature sensors.

### 2.4.1. Sensors

Industrial-grade sensors were selected to characterize the biomass gasifier prototype. These sensors feature specially designed and sealed enclosures to operate in environments with contaminants, such as dust and splashes. They also incorporate 4–20-mA industrial standard transducers, which are known for their immunity to the electromagnetic noise generated by motors [33, 34]. In the prototype, potential sources of electromagnetic noise that could negatively impact the instrumentation include the motors responsible for dislodging ash from the reactor walls, facilitating fuel descent into the combustion chamber, as well as the blower motor.

K-type thermocouples, with a temperature range of 0–1200 °C, were placed at different sections of the reactor. Additionally, a PT100 sensor, with a temperature range of 0–100 °C, was chosen to monitor the performance of the heat exchanger, ensuring that the temperature is reduced to approximately 50 °C. The PT100 sensor provides a higher resolution within its operating range than the thermocouples, justifying the change in sensor type. Differential pressure sensors coupled with properly sized Venturi tubes were used to measure the airflow at the inlet and outlet of the prototype. This setup generated a pressure variation proportional to the airflow rate (detailed calculations can be consulted in Appendix B). This combination is preferred in industrial settings for fluids prone to contamination, where other measurement devices such as rotameters are inoperative.

### 2.4.2. Actuators

To ensure efficient gasifier operation, several physical components were integrated to enhance system performance and control. The blower adjusts combustion temperature by regulating the airflow rate injected into the reactor, increasing the oxidizing agent and allowing higher combustion temperatures. Agitator motors prevent the buildup of plant-based fuel on the reactor walls, promoting its movement to the combustion zone by gravity and avoiding ash accumulation. Additionally, a T-valve connected to a chimney redirects the producer gas either for incineration in a

flare stack or to the engine intake manifold based on a test of the flame's color. The flame should turn blue to confirm that the gas is sufficiently clean and tar-free. This configuration enables real-time verification that the target reaction temperature, approximately 800 °C, has been reached.

### *2.4.3. Wireless control system*

Data collection was performed wirelessly, allowing the operators to interact with the system in real time, even in manual mode, without the need to open the sealed control unit enclosure. Despite the wireless nature of data transmission, it is crucial to maintain secure communication between the system and the computer without data loss. A web interface was developed to help visualize the data and control the various system components. Through this interface, users can access historical measurement records, calibrate sensors, adjust control parameters, and set target temperatures.

The system was designed to monitor and control the prototype autonomously, although manual ignition is required during the initial phase. All the measurements and actuator inputs were stored locally on a microSD card, complete with timestamps. With each new data collection, these measurements were updated and displayed on the user's graphical web interface, allowing for the detection of irregularities and monitoring of the system's overall performance.

The control system comprised a control unit, real-time clock (RTC), microSD card slot, connectors for the 4–20-mA sensors, power supply system, and power-consuming elements. These elements included relays for motor actuation (without regulation) and a power stage for precise control of the blower motor. A schematic diagram of the control system is illustrated in Fig. 2.

The principal component of the control unit is an ESP32 microcontroller (Espressif Systems). This system-on-chip integrates two ultralow-power processors, offering robust computational capabilities while minimizing energy consumption. ESP32 can implement multiple communication protocols, including SPI and I2C, which are essential for interfacing various sensors and actuators within a system [35, 36]. Furthermore, ESP32 supports wireless connectivity in the 2.4-GHz band, incorporating both Bluetooth and Wi-Fi transceivers, which facilitate seamless data transmission

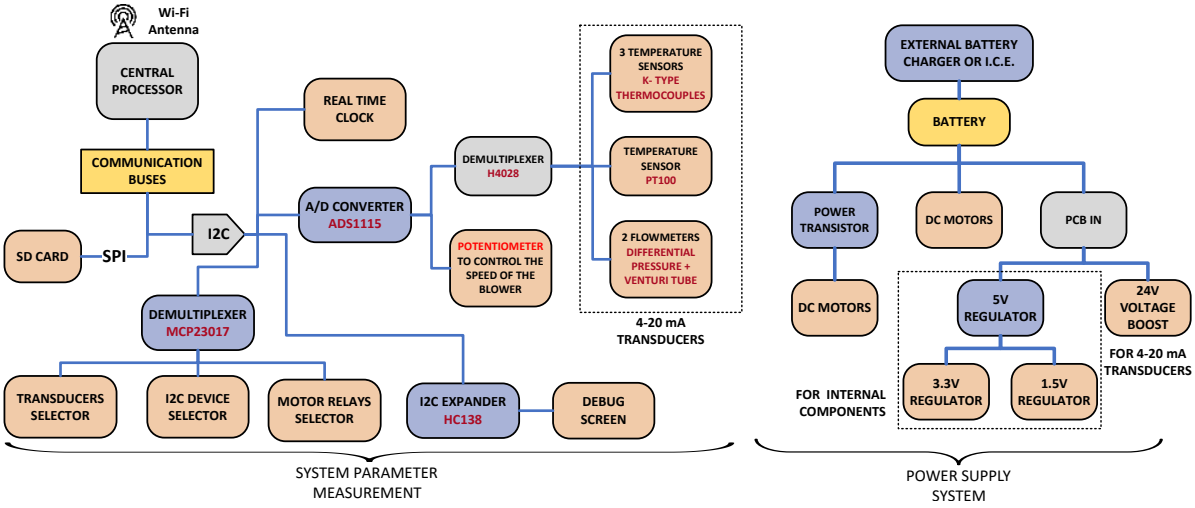


Figure 2: Schematic diagram of the main hardware elements.

and remote monitoring.

The printed circuit board (PCB) is complemented by additional key components, as shown in Fig. 3. These elements enhance the functionality and reliability of the control unit, thereby ensuring the efficient operation of the gasification system. The PCB integrates power management circuits to stabilize the supply voltage, signal conditioning modules for accurate sensor data acquisition, and communication interfaces to ensure reliable data exchange between the microcontroller and the peripheral devices.

Incorporating an ESP32 microcontroller into the control unit design provides a versatile platform capable of managing complex control tasks and real-time data processing. Its wireless communication capabilities also enable remote monitoring and control, which are critical for optimizing the performance and safety of the gasification process. The integration of these features into a compact, energy-efficient design underscores the suitability of ESP32 for industrial applications such as biomass gasification.

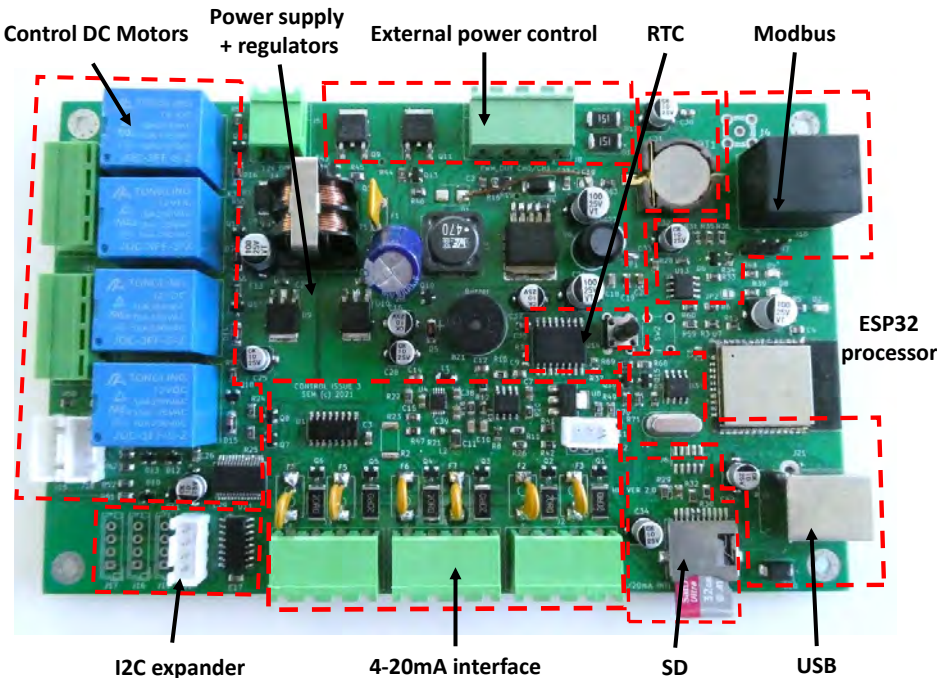


Figure 3: Prototype control unit hardware.

### 2.4.4. *Measurements of temperature and gas flow rate*

To measure the gas temperature and flow, the instrumentation system employs industrial sensors that incorporate standard 4–20-mA transceivers. These transceivers require a supply voltage of 24 V, which is provided by a voltage booster integrated into the system. Sensors consume minimal energy; therefore, a high current supply is unnecessary.

Temperature was measured inside the reactor using three K-type thermocouples located at different zones such as drying–pyrolysis, oxidation, and reduction [23, 24]. A PT100 sensor was used at the gas outlet of the system to ensure that the heat exchanger operated correctly and that the product gas could be safely introduced into the ICE without causing damage. Differential pressure sensors coupled with Venturi tubes were used to measure the inlet airflow and the synthesis gas flow at the outlet. This generates a pressure increase that is proportional to the fluid flow rate. Detailed calculations are provided in Appendix B.

To optimize the design and reduce the size of the measurement hardware, the instrumentation system employed a single ADS1115 analogue-to-digital (A/D) converter, necessitating the use of

a demultiplexer for all 4–20-mA analogue inputs.

The transceivers are not designed for immediate operation; they require a stabilization time of approximately 6 seconds after being powered, totaling approximately 36 seconds for the six sensors. To bypass this delay, a resistor connected to the negative pole of each transceiver was used to continuously power it. When a data sample is required, the transistor redirects the current from each input to the A/D converter without disrupting operation. This approach enables the instant measurement of all parameters.

To verify the behavior and linearity of the system in response to changes in the flow rate and temperature, each sensor was calibrated in the laboratory. This process included setting up different valves that redirected the airflow towards either the reactor or the exhaust. The reduction in the cross section of the air hoses was considered in the calculations because it imposes a limitation on the maximum flow rate that can be supplied by the blower.

For temperature calibration, a calibrated PT100 sensor and a type-K thermocouple (RS Amidata) were used. The differential pressure gauges were calibrated with a high-power blower, exceeding the power of the blower eventually installed in the prototype, along with a pressure meter capable of measuring up to 200 slm (12 $m^3$/h). The detailed calibration procedures conducted in the laboratory are provided in Appendix C.

### *2.4.5. Power supply system*

The system is powered by a gel battery designed for photovoltaic systems, which provides a voltage of 12 V and can supply a high current. Once electricity is generated, the battery can be charged using a photovoltaic panel or by the system itself. During the experiments, the battery was charged in the laboratory using a mobile battery charger.

The system operates at five different voltages on the printed circuit board:

- 12 V: Supplied by the battery, from which the remaining voltages in the system arise. Through a series of protective fuses, it also provides a high current to components, such

as the agitator motors responsible for ash removal and the movement of solid fuel inside the reactor, as well as feeds the transistor that regulates the blower.

- 24 V: Generated by an embedded converter (XL6009) capable of supplying up to 1A, this voltage powers the 4–20-mA transceivers. Each device is equipped with a PolyFuse (PTC-based resettable fuse) thermistor to prevent control unit issues in the event of an external short circuit, opening the circuit until the issue is resolved.
- 5, 3, and 1.5 V: These voltages are provided by AMS1117-XX linear low-dropout regulators and are used to power various integrated circuits within the system.

#### *2.4.6. Power consuming elements*

Both the motors that vibrate the reactor and the blower that drives air for combustion are powered by a 12-V battery. The motors operate using a simple on/off control mechanism implemented through relays. By contrast, the blower utilizes a PID control system that modulates the power supply using PWM and an external power transistor.

### *2.5. Firmware and software*

This section describes the software and firmware that make up the control system, including task management, interaction with the web interface, and flexible programming for process automation and real-time monitoring.

#### *2.5.1. Firmware*

To provide robustness against failures during operation and allow the parallelization of different tasks to be performed by the control unit, the FreeRTOS operating system was implemented. RTOS allows the programmer to define tasks and set execution priorities, thereby ensuring that the system works as planned. To prevent data loss, data are stored locally on a microSD card, which also supports remote access.

If the system must stop immediately, the monitoring will continue without corrupting the data as long as the power is not cut or the user stops it; therefore, turning off the system and removing

the microSD card could allow access to the information provided by the different sensors and the system to be able to locate and correct malfunctions.

The process of data acquisition and system control is composed of seven main tasks, which are illustrated in the simplified workflow diagram in Fig. 4. These tasks include Wi-Fi TCP/IP communication, firmware update, web server request processor, web socket data interchange, sensor data capture, automatic mode interpreter, and the PID power control loop.

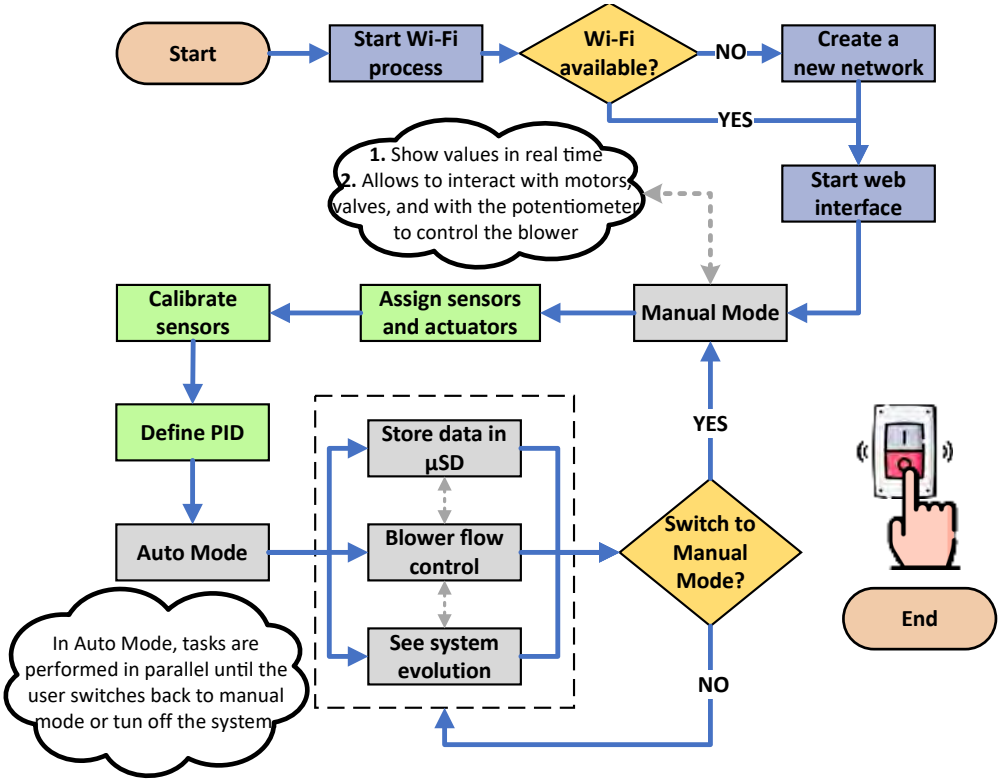


Figure 4: Schematic flowchart of the firmware operation.

Upon startup, all tasks are initialized and stored in static memory, remaining in a standby state until an event allows them to continue. Initially, the system attempts to establish a wireless connection with a known Wi-Fi network. If no connection is achieved after several attempts, the system creates a new network (access point mode) such that the user can access the control and monitoring interface provided by the internal web server. Web server pages are stored in the internal memory of the microcontroller; therefore, if the SD card is removed or damaged, the

server will continue to work. In addition, the web server allows for the review and configuration of the sensor calibration values.

By default, the system starts in manual mode, allowing the user to control the motors and inlet airflow through a remote web user interface. This manual control allows for ignition and reactor initiation. The user can also control the data acquisition. Once the gasification process inside the reactor is started, the system can be switched to automatic mode. In this mode, the control unit is responsible for maintaining the desired temperature by adjusting the inlet airflow to regulate combustion.

### *2.5.2. Software*

The control unit utilizes a programming language that allows users to define the operating time intervals for each motor. System behavior is configured using a sequential instruction-based language, such as BASIC. Users can start, stop, or modify a program interactively and remotely via a command-line interface. This customizable approach offers significant system flexibility, enabling future automation of processes such as system startup or generator control by incorporating the necessary instructions.

By default, the system operates in automatic mode, requiring no user interaction. In the event of communication loss, the system continues functioning independently. The graphical user interface provides real-time visualization of variable trends, temperature setpoint adjustment, sensor calibration, OTA updates, and remote data retrieval from the memory card. In manual mode, users can also adjust blower power as desired.

Due to the system's high thermal inertia, constant interaction with the blower's flow control is unnecessary. To save resources, measurements can be recorded every 30 seconds. However, to obtain more precise monitoring curves, measurements should be updated every second.

## 3. Results and discussion

To validate the system's functionality and its responsiveness to user demands, two field tests were conducted. The aim of both tests was to investigate the temperature behavior inside the gasifier, as well as the ability of the automated control system to maintain the target temperature. The system was fully loaded to its maximum capacity with 26.62 kg of olive pomace pellets and then started from ambient conditions (approx. 25 °C).

The first test aimed to evaluate the system's response to changes in predefined working conditions. According to the scientific literature [24], airflow rate and biomass type are the most important factors affecting the temperature in biomass gasifiers. Temperature control is relatively straightforward and depends directly upon the supplied amount of air [23]. Initially, a temperature setpoint of 600 °C was established. After the system stabilized at this temperature, the setpoint was raised to 800 °C. The transition to the higher temperature took approximately 10 minutes, during which the system maintained stability at the new temperature.

The second test focused on achieving 800 °C, starting again from ambient conditions. This temperature aligns with the typical operating conditions for temperature control in downdraft gasifiers, as documented in the scientific literature [23, 24]. Once both tests were completed, the system was opened for cleaning, and the remaining charred feedstock was weighed. Overall, 13.43 kg of biomass feedstock was consumed during the tests. The experimental setup used for the field tests is shown in Fig. 5.

During the first test, a thermal imaging camera was used to monitor the system's performance throughout the transitional phase. Fig. 6 shows four thermal images captured at different intervals, illustrating the temperature distribution along the reactor's external surface. The process began with heat generation in the combustion zone, which then propagated to the adjacent pyrolysis and gasification zones. The surface temperature peaked at 125 °C during the external heat supply via a blowtorch and stabilized around 230 °C during steady-state operation. The significant temperature gradient observed between the interior (800 °C) and the exterior (230 °C) of the gasification reactor

Figure 5: Images of the reactor prototype, including a close-up view of the control system.

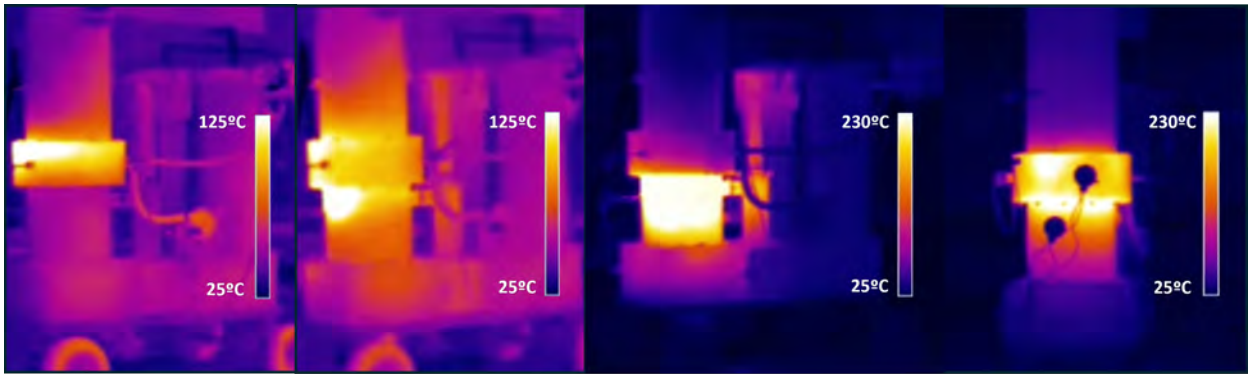


*a)* *b)* *c)* *d)*

Figure 6: *a)* Combustion zone during startup *b)* Temperature distribution in the reactor within approximately 30 minutes from startup *c)* Temperature distribution in the reactor around one hour after startup *d)* Temperature distribution in the reactor during steady-state operation showing the placement of thermocouples.

reflects the system's high insulation efficiency.

### *3.1. System performance during the first startup phase*

The initial startup was conducted on May 27, 2024, to evaluate whether the control system could maintain a stable temperature in the reactor's central zone. During this test, the temperature was initially set to approximately 600 °C, with a tolerance of ±25 °C, before being raised to a final target of 800 °C. The behavior observed in this test is presented in Fig. 7 a), where significant

variations in temperature readings are observed across different zones of the reactor. Specifically, the temperatures in the lower, middle, and upper zones varied considerably, with sensors placed just 30 cm apart, while the producer gas outlet temperature remained consistently stable at around 40 °C.

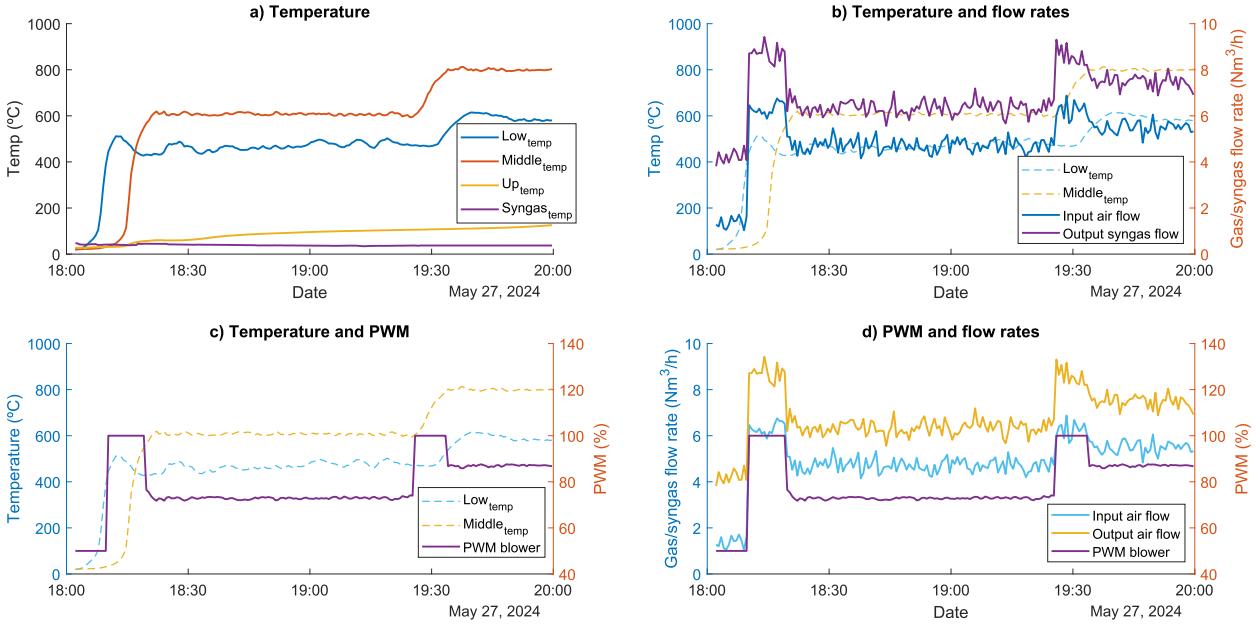


Figure 7: Temperatures, air and product gas, and PWM recorded during the first startup.

Manual intervention is necessary to operate the gasification system, as roughly 75% of the incoming air flow is rerouted to the outlet via a T-valve. This redirection generates a vacuum effect that drives combustion gases through the cooling and cleaning stages while also ensuring that the flare remains ignited.

After seven and a half minutes, the gasification temperature of 400 °C in the reduction zone at the reactor's lower section was reached, at which point the automatic mode could be activated. In automatic mode, the system first aims to reach the target temperature by increasing air intake to promote combustion, as reflected by the initial sharp flow increase in Fig. 7 b). Subsequently, the airflow rate is regulated to maintain the setpoint temperature until deactivation, shutdown, or the establishment of a new operating temperature.

Flow measurement exhibits significant noise due to the inherent nature of the flow sensing system, which is subject to constant pressure fluctuations. These variations arise from the blower blade position, which may either have just passed or be actively pushing air at each capture point. For a comprehensive overview, Fig. 7 c) and d) illustrate the control signal alongside the resulting changes in temperature and flow rates in the reduction and combustion zones during the first startup.

### *3.2. System performance during the second startup phase*

The second startup aimed to replicate a more realistic operating condition by directly targeting a set-point temperature of 800 ± 25 °C in the combustion zone. Automatic mode was activated after an 8-minute startup phase. The system reached the target temperature within 16 minutes and stabilized it in approximately 3 additional minutes, maintaining a uniform temperature for the entire two-hour test duration. The temperature behavior throughout the process is shown in Fig. 8 a). Similar to the first startup, the temperatures in the lower, middle, and upper zones of the reactor are presented, along with the producer gas temperature at the reactor outlet.

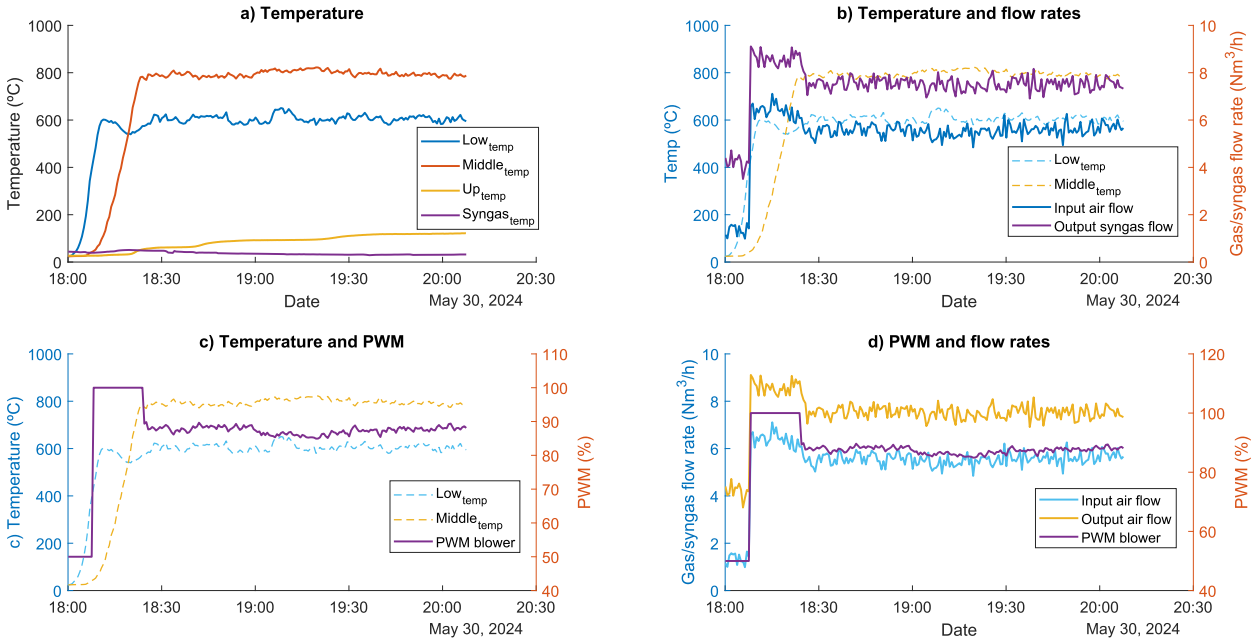


Figure 8: Temperatures, air and product gas, and PWM recorded during the second startup.

As also observed during the first test, Fig. 8 b) reveals some instability in airflow measurements caused by minor pressure fluctuations inherent to the blower's operation, which did not significantly affect system performance. Despite this slight instability induced by the blower, the control signal analysis in Fig. 8 c) and d) indicates minimal variation between input and output temperatures and flow rates, demonstrating an overall stable and reliable system performance.

## 4. Conclusions and future outlook

Gasification demonstrates substantial potential for the utilization of agricultural waste. As demonstrated in this study, monitoring and automated control systems facilitate the use of this technology and can support electrification in off-grid areas, such as remote or isolated regions (including rural areas), due to its low cost, ease of handling and maintenance, and adaptability to various biomass sources. Additionally, optimizing operational parameters enhances process efficiency, maximizing energy conversion while reducing emissions. These advancements strengthen its viability as a sustainable alternative, with applications in both distributed generation and microgrid integration.

The ESP32-based control system with FreeRTOS not only efficiently manages the gasification process, but also possesses computational capacity beyond immediate needs. This means that while the system awaits key events, its processor has ample resources to handle additional tasks without compromising performance. Thanks to these features, it is possible to integrate additional sensors (such as two 4–20 mA sensors), expand communication with I2C devices, and even coordinate two gasifiers simultaneously via wireless connectivity or the Modbus protocol, which is widely used in industry. Beyond energy management optimization, this capability also enables the implementation of a parallel redundant system, ensuring continuous operation in case of failures or maintenance. All of this can be achieved without major modifications to the current design, reinforcing the flexibility and scalability of the solution. Finally, remote access through an intuitive mobile interface not only simplifies system operation, but also bridges the gap between technology

and its users.

## Nomenclature

### Abbreviations

| | |
|---|---|
| A/D | Analog to digital |
| ANFIS | Adaptive neuro-fuzzy inference system |
| FIS | Fuzzy inference system |
| FLC | Fuzzy logic controller |
| I2C | Inter-integrated circuit |
| ICE | Internal combustion engine |
| MIMO | Multi-input multi-output |
| OTA | Over the air |
| PCB | Printed circuit board |
| PID | Proportional integral derivative |
| PSO | Particle swarm optimization |
| PTC | Positive temperature coefficient |
| PWM | Pulse width modulation |
| RTC | Real-time clock |
| RTOS | Real-time operating system |
| SPI | Serial peripheral interface |

## Credit authorship contribution statement

**A. Rodríguez Orta:** Conceptualization, Data curation, Formal analysis, Investigation, Methodology, Software, Validation, Visualization, Writing - Original Draft, Writing - Review & Editing. **M. Sánchez Raya:** Conceptualization, Formal analysis, Investigation, Methodology, Software, Validation. **R. Aguado Molina:** Conceptualization, Formal analysis, Investigation, Methodology, Validation, Visualization, Writing - Original Draft, Writing - Review & Editing. **D. Vera Candeas:** Conceptualization, Funding acquisition, Project administration, Resources, Supervision, Validation, Writing - Review & Editing. **J.A. Gómez Galán:** Conceptualization, Funding acquisition, Resources, Supervision, Validation, Writing - Review & Editing. **D.A. López García:** Conceptualization, Formal analysis, Investigation, Validation.

## Declaration of competing interest

The authors declare that they have no known competing financial interests or personal relationships that could have appeared to influence the work reported in this paper.

## Funding

This research work was supported by the project entitled "Renewable energies for Africa: Effective valorisation of agri-food wastes (REFFECT AFRICA)", which has received funding from the *European Union's Horizon 2020 Research and Innovation Programme* under the following Grant Agreement ID number: 101036900.

## References

[1] R. Aguado, D. Vera, D. A. López-García, J. P. Torreglosa, F. Jurado, Techno-economic assessment of a gasification plant for distributed cogeneration in the agrifood sector, Appl. Sci. 11 (2) (2021). doi:10.3390/app11020660.

[2] P. Basu, Biomass gasification, pyrolysis and torrefaction: Practical design and theory, Elsevier, 2018. doi:10.1016/C2016-0-04056-1.

[3] D. Vera, F. Jurado, K. D. Panopoulos, P. Grammelis, Modelling of biomass gasifier and microturbine for the olive oil industry, Int. J. Energy Res. 36 (3) (2012) 355–367. doi:10.1002/er.1802.

[4] D. Vera, F. Jurado, N. K. Margaritis, P. Grammelis, Experimental and economic study of a gasification plant fuelled with olive industry wastes, Energy Sustain. Dev. 23 (2014) 247–257. doi:10.1016/j.esd.2014.09.011.

[5] R. Aguado, A. Escámez, F. Jurado, D. Vera, Experimental assessment of a pilot-scale gasification plant fueled with olive pomace pellets for combined power, heat and biochar production, Fuel 344 (2023) 128127. doi:10.1016/j.fuel.2023.128127.

[6] C. Higman, M. V. der Burgt, Gasification, Gasification (2008) 1–435doi:10.1016/B978-0-7506-8528-3.X0001-6.

[7] F. Y. Hagos, A. R. A. Aziz, S. A. Sulaiman, Trends of syngas as a fuel in internal combustion engines, Adv. Mech. Eng. 6 (2014) 401587. doi:10.1155/2014/401587.

[8] A. V. Bridgwater, The technical and economic feasibility of biomass gasification for power generation, Fuel 74 (1995) 631–653. doi:10.1016/0016-2361(95)00001-L.

[9] P. R. Bhoi, R. L. Huhnke, A. Kumar, S. Thapa, N. Indrawan, Scale-up of a downdraft gasifier system for commercial scale mobile power generation, Renew. Energy 118 (2018) 25–33. doi:10.1016/j.renene.2017.11.002.

[10] A. Kushwah, T. Reina, M. Short, Modelling approaches for biomass gasifiers: A comprehensive overview, Sci. Total Environ. 834 (2022) 155243. doi:10.1016/j.scitotenv.2022.155243.

[11] M. Asadullah, Barriers of commercial power generation using biomass gasification gas: A review, Renew. Sust. Energ. Rev. 29 (2014) 201–215. doi:10.1016/j.rser.2013.08.074.

[12] E. Shayan, V. Zare, I. Mirzaee, Hydrogen production from biomass gasification; a theoretical comparison of using different gasification agents, Energy Convers. Manag. 159 (2018) 30–41. doi:10.1016/j.enconman.2017.12.096.

[13] S. Heidenreich, M. Müller, P. U. Foscolo, Advanced biomass gasification: New concepts for efficiency increase and product flexibility, Advanced Biomass Gasification: New Concepts for Efficiency Increase and Product Flexibility (2016) 1–134doi:10.1016/C2015-0-01777-4.

[14] D. Thimsen, R. Maurer, A. Pooler, D. Pui, B. Liu, D. Kittelson, Fixed-bed gasification research using US coals. Volume 14. Gasification of Kemmerer subbituminous coal, Bureau of Mines United States Department of the Interior, 1985. doi:10.2172/5868732.

[15] M. Dogru, Experimental results of olive pits gasification in a fixed bed downdraft gasifier system, Int. J. Green Energy 10 (4) (2013) 348–361. doi:10.1080/15435075.2012.655351.

[16] T. K. Patra, P. N. Sheth, Biomass gasification models for downdraft gasifier: A state-of-the-art review, Renew. Sust. Energ. Rev. 50 (2015) 583–593. doi:10.1016/j.rser.2015.05.012.

[17] A. Molino, S. Chianese, D. Musmarra, Biomass gasification technology: The state of the art overview, J. Energy Chemistry 25 (2016) 10–25. doi:10.1016/j.jechem.2015.11.005.

[18] D. Baruah, D. C. Baruah, Modeling of biomass gasification: A review, Renew. Sust. Energ. Rev. 39 (2014) 806–815. doi:10.1016/j.rser.2014.07.129.

[19] S. K. Sansaniwal, K. Pal, M. A. Rosen, S. K. Tyagi, Recent advances in the development of biomass gasification technology: A comprehensive review, Renew. Sust. Energ. Rev. 72 (2017) 363–384. doi:10.1016/j.rser.2017.01.038.

[20] C. Sagüés, P. García-Bacaicoa, S. Serrano, Automatic control of biomass gasifiers using fuzzy inference systems, Bioresour. Technol. 98 (4) (2007) 845–855. doi:10.1016/j.biortech.2006.03.004.

[21] A. S. Gandhi, T. Kannadasan, R. Suresh, Biomass downdraft gasifier controller using intelligent techniques, in: Y. Yun (Ed.), Gasification for Practical Applications, IntechOpen, 2012. doi:10.5772/48564.

[22] B. Gøbel, U. Henriksen, T. K. Jensen, B. Qvale, N. Houbak, The development of a computer model for a fixed bed gasifier and its use for optimization and control, Bioresour. Technol. 98 (10) (2007) 2043–2052. doi:10.1016/j.biortech.2006.08.019.

[23] N. Striūgas, K. Zakarauskas, A. Džiugys, R. Navakas, R. Paulauskas, An evaluation of performance of automatically operated multi-fuel downdraft gasifier for energy production, Appl. Therm. Eng. 73 (1) (2014) 1151–1159. doi:10.1016/j.applthermaleng.2014.09.007.

[24] P. V. Daniel, A. S. Gandhi, Enhanced conventional PID controller for temperature control in woody gasifier using searching algorithms, International Journal of Innovative Technology and Exploring Engineering (IJITEE) (4) (2019) 438–442.
URL https://www.ijitee.org/wp-content/uploads/papers/v8i4s/DS2903028419.pdf

[25] V. S. Sikarwar, M. Zhao, P. S. Fennell, N. Shah, E. J. Anthony, Progress in biofuel production from gasification, Prog. Energy Combust. Sci. 61 (2017) 189–248. doi:10.1016/j.pecs.2017.04.001.

[26] M. L. V. Rios, A. M. González, E. E. S. Lora, O. A. A. del Olmo, Reduction of tar generated during biomass gasification: A review, Biomass and Bioenergy 108 (2018) 345–370. doi:10.1016/J.BIOMBIOE.2017.12.002.

[27] A. Escámez, R. Aguado, D. Sánchez-Lozano, F. Jurado, D. Vera, An ensemble multi-ANN approach for virtual oxygen sensing and air leakage prediction in biomass gasification plants, Renew. Energy 242 (2025) 122376. doi:10.1016/j.renene.2025.122376.

[28] C. Huang, S. Wang, Y. Chu, Y. Chen, X. Chen, L. Liu, H. Zhang, Comprehensive investigations on the explosion suppression of biomass fuels: Starch as a representative, Fuel 315 (2022) 123276. doi:10.1016/j.fuel.2022.123276.

[29] G. Liang, H. Dai, H. Yin, Q. Zhao, X. Chen, Inhibition characteristics of coal dust explosion at the gasification atmosphere, Advanced Powder Technology 32 (2021). doi:10.1016/j.apt.2021.08.026.

[30] S. Lin, Z. Liu, J. Qian, X. Li, Comparison on the explosivity of coal dust and of its explosion solid residues to assess the severity of re-explosion, Fuel 251 (2019). doi:10.1016/j.fuel.2019.04.080.

[31] A. Gagliano, F. Nocera, M. Bruno, G. Cardillo, Development of an equilibrium-based model of gasification of biomass by Aspen Plus, Energy Procedia 111 (2017) 1010–1019. doi:10.1016/j.egypro.2017.03.264.

[32] R. Aguado, D. Vera, F. Jurado, G. Beltrán, An integrated gasification plant for electric power generation from wet biomass: toward a sustainable production in the olive oil industry, Biomass Conv. Bioref. (2022). doi:10.1007/s13399-021-02231-0.

[33] P. P. Divyang, V. Mehta, Design of high accurate universal intelligent temperature transmitter, IJSTE-International Journal of Science Technology & Engineering 4 (2018) 162–168.

[34] T. Witt, R. Mena, E. Cornell, Single chip, 2-wire, 4–20 mA current loop RTD temperature transmitter design, IECON Proceedings (Industrial Electronics Conference) (2014) 2380–2383doi:10.1109/IECON.2014.

7048837.

[35] M. Tabaa, B. Chouri, S. Saadaoui, K. Alami, Industrial Communication based on Modbus and Node-RED, Procedia Computer Science 130 (2018) 583–588, the 9th International Conference on Ambient Systems, Networks and Technologies (ANT 2018) / The 8th International Conference on Sustainable Energy Information Technology (SEIT-2018) / Affiliated Workshops. doi:10.1016/j.procs.2018.04.107.

[36] P. Neumann, Communication in industrial automation—What is going on?, Control Engineering Practice 15 (11) (2007) 1332–1347, special Issue on Manufacturing Plant Control: Challenges and Issues. doi:10.1016/j.conengprac.2006.10.004.

## Appendix A. Verification of the linearity of the analog-to-digital converter

### *A.1. Electronic components configuration*

The different sensors incorporated in the prototype use the 4–20-mA industrial communications protocol, which corresponds to the start and full scale of each transducer. Below are the locations of the different sensors incorporated into the prototype and their measurement ranges.

#### *A.1.1. Temperature in all three reactor sections*

The reactor is designed for high-temperature gasification, with temperatures expected to oscillate around 800 °C. Temperature is measured with K-type thermocouples, which have a measurement range of 0 to 1000 °C (corresponding to 4 and 20 mA, respectively). With these thermocouples, the expected temperature range is fully covered, leaving a small margin for when the temperature exceeds the set point during the stabilization stage.

#### *A.1.2. Temperature of the product gas at the outlet of the treatment system*

The producer gas conditioning system was designed to obtain a suitable temperature for the engine generator. The PT100 sensor, which measures between 0 and 100 °C, covers the system's operating range, with 4 mA corresponding to 0 °C and 20 mA to 100 °C.

#### *A.1.3. Reactor inlet air flow or producer gas outlet air flow*

Based on the reactor design stage, the reactor is expected to operate with the inlet air and outlet product gas flows of up to 50 $m^3$/h. A standardized flow measurement system, commonly used in industry, was implemented using a Venturi tube in combination with a differential pressure meter. It was dimensioned to create a pressure differential such that the differential pressure gauge, which could measure from 0–500 Pa, obtained a maximum reading of 78.6 $m^3$/h. This was higher than the expected range according to the simulation software. These calculations are specified in Appendix B.

To transform the measurements provided by different transducers into a binary value usable by the control unit, a 16-bit analogue-to-digital (A/D) converter, ADS1115, was employed. The problem with its direct implementation is that the converter is designed to measure voltages rather than currents. To solve this problem, a 20 Ω± 5% resistor was placed at each input of the system as a shunt resistor, allowing voltage measurements to be converted to current by applying Ohm's law.

With the default configuration provided by the manufacturer, the A/D converter can measure from 0 to 165 mA, considering that its power supply is 3.3 V. This range provides a low resolution for current measurement in the range of 4–20 mA, despite the large number of bits of the converter (16 bits). As an alternative to adjusting the system and fine-tuning the measurement, an operational amplifier (op-amp) in the single-ended mode, ADA4940, was used. In Fig. A.1, the lector is shown as a symbolic diagram related to the A/D converter.

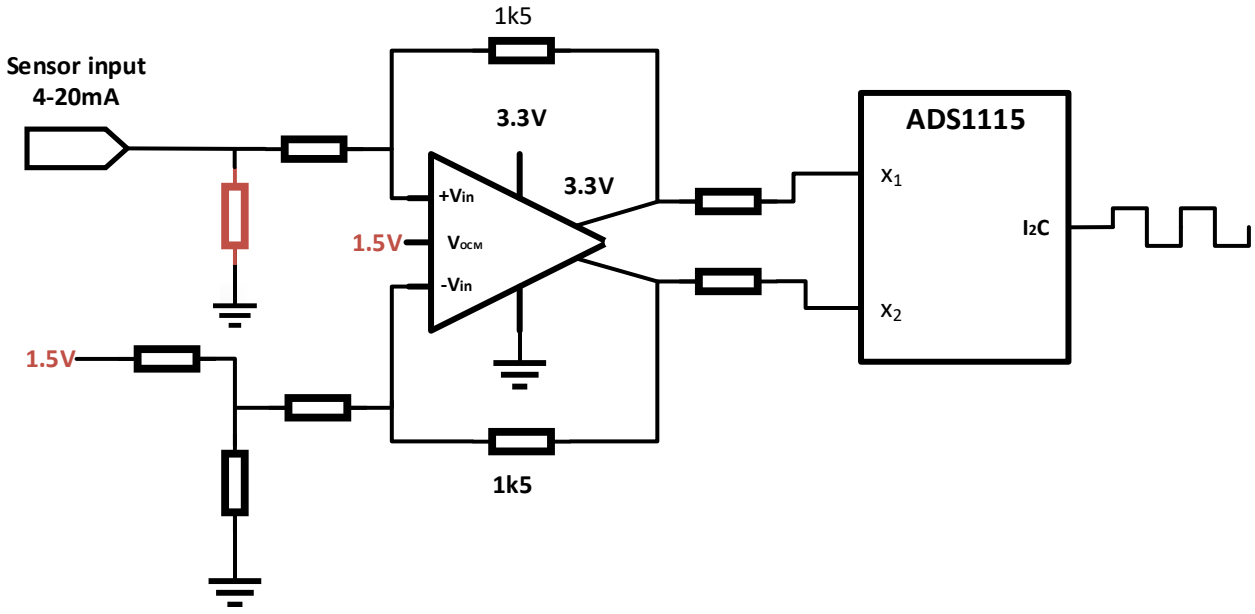


Figure A.1: Setting used to adjust the scaling of the analog to digital converter, ADS1115.

The op-amp was designed and adjusted to convert the 4–20-mA signal to 0–3.3 V. This requires the incorporation of a precision voltage regulator at 1.5 V, which sets the power supply range for the comparison of the inputs, as well as a low impedance voltage divider, which sets the negative

input of the comparator at 0.232 V (voltage obtained using simulation software).

The instrumentation system has a ground island separated from the rest by a 100-µH coil to avoid introducing the electrical noise produced by the switched voltage booster, which supplies power to the different transducers (12 V from the battery to 24 V) in the instrumentation circuitry. For such isolation to be effective, low impedance (22 Ω resistor connected to the ground) must be available.

The elements connected in a separate ground zone must be configured such that the injection current does not exceed 50 mA for the entire assembly process. Therefore, we decided to limit this current to 15 mA in the case of the voltage divider connected to the -Vin input of the op-amp. If Ohm's law is applied with the components shown in Fig. A.1, a current of 10.42 mA is obtained. This value is lower than the intended current, which ensures proper separation of the ground.

$$I_{divisor} = \frac{1.5\,\mathrm{V}}{(120 + 24)\,\Omega} = \frac{1.5\,\mathrm{V}}{144\,\Omega} = 10.42\,\mathrm{mA} \tag{A.1}$$

The selection of the different components of the circuit (shown in Fig. A.1) has been made following the indications provided by the Diff-Amp Calculator software of the Op-amp manufacturer (Analog Devices). Fig. A.2 shows the configuration entered in the software, together with the expected output of the amplifier for a target gain of 7 ($V_{out}/V_s$).

### *A.2. Test system assembly*

Laboratory testing of the system for the operating ranges of different sensors (4–20 mA) was performed using a prototyping board comprising six voltage dividers. Each divider is composed of a 1-kΩ precision resistor (±1%) and a 5-kΩ potentiometer. The calculations justifying this selection are as follows:

$$V_{zero} = 0.004\,\mathrm{A} \cdot 20\,\Omega = 0.4\,\mathrm{V} \rightarrow R_{max} = \frac{24\,\mathrm{V} - 0.4\,\mathrm{V}}{0.004\,\mathrm{A}} = 5900\,\Omega \tag{A.2}$$

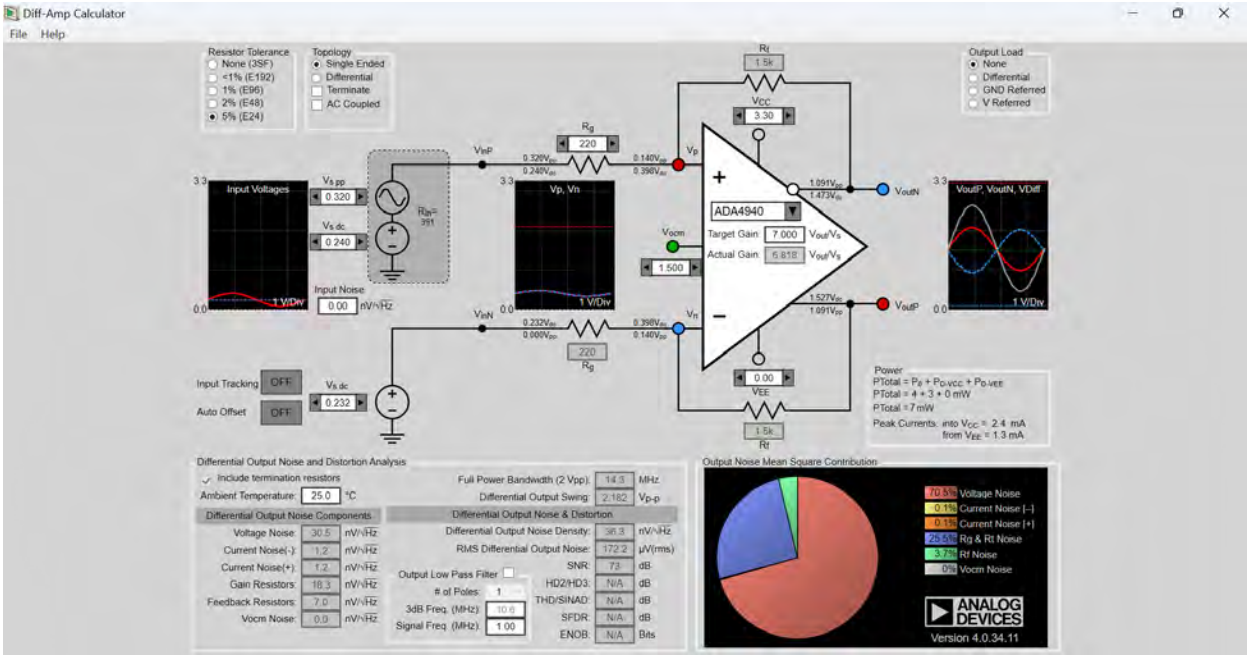


Figure A.2: Configuration obtained with the Analog Devices software.

$$V_{fullscale} = 0.02\,\text{A} \cdot 20\,\Omega = 0.08\,\text{V} \rightarrow R_{min} = \frac{24\,\text{V} - 0.08\,\text{V}}{0.02\,\text{A}} = 1196\,\Omega \tag{A.3}$$

The following laboratory instruments were used to evaluate the assembly, as discussed in the previous section. The laboratory instruments used in this study are shown in Fig.A.3.

- Power source MLINK APS3005S-3D supplies a supply voltage of 12 V, emulating the behavior of the power supply battery of the system.
- Agilent 340405 multimeter used to measure the voltage drop across the 20 Ω shunt resistor.
- TTi 1705 multimeter for measuring the current through the reference resistor.

### *A.3. Empirical data obtained in laboratory*

With the setup discussed in subsections a) and b), the start and full-scale values of 3.2 and 21.83 mA, corresponding to the A/D converter measurements of 12,206 and 49,384, respectively, were obtained. Once the start and end of the measurement range were known, measurements were performed within this range. The measurements are listed in Table A.1:


Figure A.3: Laboratory equipment used.

Table A.1: Laboratory readings.

| Multimeter current (mA) | Binary readings | Voltage (mV) |
|---|---|---|
| 4.09 | 13932 | 81.66 |
| 5.01 | 15778 | 100.03 |
| 6.01 | 17758 | 119.91 |
| 7.01 | 19768 | 140.04 |
| 8.01 | 21742 | 159.73 |
| 9.04 | 23780 | 180.35 |
| 10.04 | 25779 | 200.21 |
| 11.01 | 27725 | 219.56 |
| 12.02 | 29723 | 239.30 |
| 13.03 | 31774 | 260.03 |
| 14.08 | 33823 | 280.48 |
| 15.08 | 35840 | 300.54 |
| 16 | 37655 | 318.71 |
| 17 | 39641 | 342.52 |
| 18.09 | 41760 | 360.54 |

Next, the current-versus-voltage reading (mV) and the current-versus-value returned by the A/D converter were plotted. These measurements were performed to check whether the instrumentation system behaved in a linear manner or whether it was necessary to make a stepwise adjustment of the returned reading. Considering the tolerance of the different passive elements,

643 circuitry was incorporated to improve the resolution of the system within a known reading range
644 (4–20 mA).

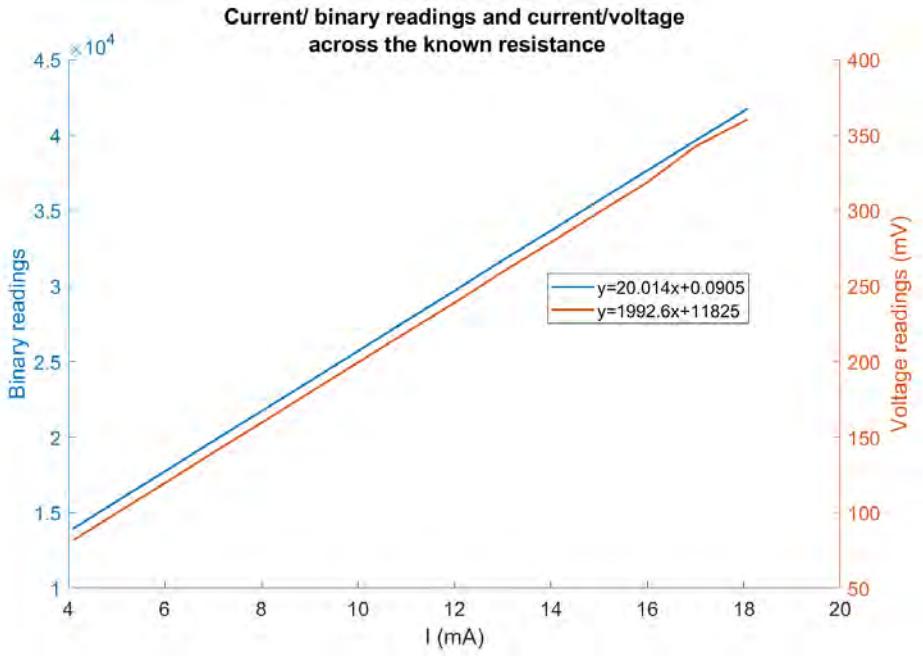


Figure A.4: Representation of the linearity of the voltage readings (mV) and the binary reading for the range 4 to 20 mA.

645 From the data shown in Table A.1, a series of conversions were performed to transform the
646 binary readings to milliamperes. The results are listed in Table A.2, considering the following
647 criteria:

648 1. Considering the number of bits of the A/D converter: The A/D converter has 16 bits such
649 that, for the measurement range of 4–20 mA, up to 65,536 combinations can be obtained.
650 The results obtained using this criterion were recorded in the column labeled “I (mA) full
651 range”.

652 When using the empirically obtained values, errors due to the tolerance of the passive el-
653 ements and accessory circuitry connected to the A/D converter are considered. Data ob-
654 tained from this transformation are presented in the column labeled “Current (mA) cali-
655 brated range”.

As a result, an average error of 2.87952445 mA was obtained with respect to the measurement provided by the TTi multimeter, which was significantly lower than that obtained using the previous criterion.

2. Starting from the criterion of the previous section, but subtracting from each measurement the average error, obtained with this criterion. The results are presented in the column labeled "Corrected value (mA)".

   The average error is 0 mA with respect to the multimeter reading. Therefore, this is the most interesting alternative. This conversion would be applied at the code level.

Table A.2: Results obtained with the different adjustment criteria for current measurements.

| Multimeter current (mA) | Full range (mA) | Reference value vs. full range (mA) | Calibrated current range (mA) | Ref. vs. calibrated value (mA) | Corrected value (mA) | Ref. vs. corrected value (mA) |
|---|---|---|---|---|---|---|
| 4.09 | 3.40 | 0.69 | 6.981364248 | 2.891364248 | 4.101839798 | -0.011839798 |
| 5.01 | 3.85 | 1.16 | 7.906400022 | 2.896400022 | 5.026875572 | -0.016875572 |
| 6.01 | 4.34 | 1.67 | 8.898583571 | 2.888583571 | 6.019059121 | -0.009059121 |
| 7.01 | 4.83 | 2.18 | 9.905800204 | 2.895800204 | 7.026275754 | -0.016275754 |
| 8.01 | 5.31 | 2.70 | 10.89497714 | 2.884977137 | 8.015452687 | -0.005452687 |
| 9.04 | 5.81 | 3.23 | 11.91622465 | 2.876224649 | 9.036700199 | 0.003299801 |
| 10.04 | 6.29 | 3.75 | 12.91792915 | 2.877929152 | 10.0384047 | 0.001595298 |
| 11.01 | 6.77 | 4.24 | 13.89307521 | 2.883075206 | 11.01355076 | -0.003550756 |
| 12.02 | 7.26 | 4.76 | 14.89427861 | 2.874278606 | 12.01475416 | 0.005245844 |
| 13.03 | 7.76 | 5.27 | 15.92204045 | 2.892040454 | 13.042516 | -0.012516004 |
| 14.08 | 8.26 | 5.82 | 16.9488001 | 2.868800097 | 14.06927565 | 0.010724353 |
| 15.08 | 8.75 | 6.33 | 17.95952445 | 2.87952445 | 15.08 | 0 |
| 16 | 9.19 | 6.81 | 18.86902604 | 2.869026037 | 15.98950159 | 0.010498413 |
| 17 | 9.68 | 7.32 | 19.8642162 | 2.864216203 | 16.98469175 | 0.015308247 |
| 18.09 | 10.20 | 7.89 | 20.92605304 | 2.836053042 | 18.04652859 | 0.043471408 |
| | Average error | 4.24 | average error | 2.87952445 | Average error | 0 |

In view of these results, it is important to note that, with correct calibration, it is possible to eliminate the errors by the tolerance of the different elements of the system to a great extent, obtaining results that are close to the target values.

This methodology is applied in the following sections to obtain a more adequate calibration of the sensors and values closer to those obtained using more specialized measuring elements.

## Appendix B. Calibration of the differential pressure meter and Venturi tube

### *B.1. Theoretical foundation*

The fluid flow rate was measured using an assembly called a Venturi tube. This device creates a pressure difference owing to the reduction in the cross section of the apparatus. As the cross section of the conductor decreases, the velocity increases, causing a decrease in pressure.

The fundamental principles underlying the Venturi tube are governed by Bernoulli's equation and the continuity equation, which represents the conservation of mass. Fig. B.1 illustrates the pressure drop resulting from the variation in velocity and cross-sectional area of a Venturi tube:

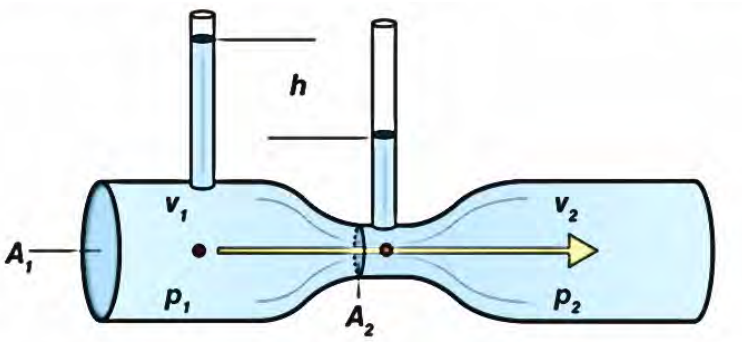


Figure B.1: Typical arrangement of a Venturi tube.

The process for determining the volumetric flow rate through this arrangement as a function of the pressure drop is described next.

- **Bernoulli equation.**

$$\frac{v_1^2}{2g} + \frac{P_1}{\gamma} + z_1 = \frac{v_2^2}{2g} + \frac{P_2}{\gamma} + z_2 \tag{B.1}$$

  where:

  - $v_i$ = fluid velocity in zone i (m/s).
  - $P_i$ = pressure exerted by the fluid in zone $i$ (in Pa or $\frac{\text{kg}}{\text{m} \cdot \text{s}^2}$).
  - $z_i$: height (m) at the nozzle of zone $i$. An apparatus capable of measuring pressure should be placed.

- $\gamma$: specific weight of the fluid $\left(\frac{\text{kg}}{\text{m}^2 \cdot \text{s}^2}\right)$, where $\gamma = \rho \cdot g$ (specific weight = density multiplied by gravity).
- $g$: acceleration of gravity (9.81 m/s$^2$).

Since the measuring nozzles were placed at the same height ($z_1 = z_2$), Eq. (B.1) can be expressed as follows:

$$\frac{v_1^2}{2g} + \frac{P_1}{\gamma} = \frac{v_2^2}{2g} + \frac{P_2}{\gamma} \tag{B.2}$$

By substituting $\gamma$ with $\rho \cdot g$, Eq. (B.3) is obtained.

$$v_1^2 - v_2^2 = \frac{2}{\rho} \cdot (P_2 - P_1) \tag{B.3}$$

- **Continuity equation or conservation of mass.**

$$Q = v_1 \cdot A_1 = v_2 \cdot A_2 \tag{B.4}$$

where:

- $Q$ is the flow rate (m/s).
- $A_i$ is the area in section $i$.
- $v_i$ is the fluid velocity in section $i$.

By clearing $v_1$ or $v_2$ from the mass conservation Eq. (B.4), the following relationships are obtained:

$$v_1 = v_2 \cdot \frac{A_2}{A_1} \tag{B.5}$$

$$v_2 = v_1 \cdot \frac{A_1}{A_2} \tag{B.6}$$

- **Fluid velocity as a ratio between pressure difference and Venturi sections.** By incorporating the relationship shown in Eqs. (B.5) and (B.6) into Eq. (B.4), Eqs. (B.7) and (B.8) are obtained:

$$v_1 = A_2 \sqrt{\frac{2 \cdot (P_2 - P_1)}{\rho \cdot (A_2^2 - A_1^2)}} = \sqrt{\frac{2 \cdot (P_2 - P_1)}{\rho \cdot \left(1 - \left(\frac{A_1}{A_2}\right)^2\right)}} \tag{B.7}$$

$$v_2 = A_1 \sqrt{\frac{2 \cdot (P_2 - P_1)}{\rho \cdot (A_1^2 - A_2^2)}} = \sqrt{\frac{2 \cdot (P_2 - P_1)}{\rho \cdot \left(\left(\frac{A_2}{A_1}\right)^2\right) - 1)}} \tag{B.8}$$

To obtain the results, it was assumed that the pressure increases and the area difference is such that the square root yields a positive result. An interesting aspect of these relationships is the ability to detect the fluid flow rate, which can be determined from a known pressure difference, or the pressure difference can be calculated as a function of the flow rate.

### *B.2. Venturi performance equations*

The volumetric flow was obtained by incorporating the relations obtained using Eqs. (B.7) and (B.8) into the continuity Eq. (B.4):

$$Q = A_1 \, v_1 = A_2 \, v_2 = A_1 \, A_2 \sqrt{\frac{2 \, (P_2 - P_1)}{\rho \left(A_2^2 - A_1^2\right)}} \tag{B.9}$$

By manipulating Eq. B.9, the pressure difference in the Venturi tube can be determined for a known flow rate and dimensions. This relationship is presented in Eq. B.10 as follows.

$$\Delta P = P_1 - P_2 = \frac{Q^2 \rho \left(A_1^2 - A_2^2\right)}{2 A_1^2 A_2^2} \tag{B.10}$$

### *B.3. Venturi tube specifications*

The Venturi tube to be calibrated in the laboratory was the same as that mounted on the prototype of the portable gasifier. It was designed to satisfy the design requirements by measuring an air or product gas flow of up to 50 $m^3$/h. This flow is significantly lower than that usually measured using commercial Venturi tubes; therefore, a tube was created using three-dimensional printing.

To conduct digital measurements of the differential pressure, a differential pressure meter with an operating range of 0–500 Pa was used. Consequently, a Venturi tube with a larger diameter of 5 cm and a smaller diameter of 3 cm was created.

For a flow rate of 50 $m^3$/h expected according to the simulations, a pressure difference of 202.31 Pa would be obtained by applying Eq. (B.10) to the Venturi tube described above. Therefore, exceeding this pressure during the calibration process is not necessary.

## Appendix C. Laboratory experimental setup

### *B.1. Temperature calibration*

Calibration must be regularly conducted to ensure that the measurements shown correspond to reality, considering the casuistry of the time and place where the experimentation will be conducted (because the system will be started outdoors, and environmental conditions cannot be controlled). For this purpose, a calibration process was repeated each time the temperature values were sampled accurately. This was first conducted in the laboratory and then in a reactor prototype.

Because the process was the same for different temperature transducers, it was executed on a single occasion in the laboratory. For this purpose, the equipment described in Appendix A was used together with a K-type thermocouple connected to a 4–20 mA transducer that is factory set with an operating range of 0–600 °C, and a heat gun with adjustable temperature. This blower is part of a soldering station. This device simulates the behavior of the system at temperatures between 100 °C and 450 °C (minimum and maximum temperatures that can be introduced into the control screen).

In addition, measurements performed by the system at ambient temperature prior to the measurement process were considered. Temperature data were obtained from a small weather station located in the laboratory. The setup used to obtain different measurements is shown in Fig. C.1:

The sampling procedure is as follows:

- First, the temperature of the hot-air soldering station was set, and the air flow was directed towards the sensor end.

  To obtain a uniform temperature distribution at the tip of the thermocouple, the nozzle was removed and the dial controlling the airflow of the blower element was set at the middle of its scale. This ensures that the air flow is directed over the entire sensitive element but prevents the blower effect from producing sudden changes in temperature. These changes are attributed to small deviations in the flow direction, causing instability in the measurements.

a) b) c)

Figure C.1: Temperature measurement setup. a) Type K thermocouple plus transducer. b) Hot air soldering station. c) Control system connection.

- Once the current reading stopped increasing for a fixed temperature value, the results obtained by the multimeter and A/D converter were recorded.

- This process was repeated with 50 °C temperature increments between measurements, until the temperature limit that the blower can produce was reached.

  The temperature indicated on the heating-element display refers to the set point obtained by the heating element. However, this does not imply that the temperature reached by the thermocouple must be the same, particularly considering the temperature diffusion performed by the heat gun because of the blowing element. Therefore, the value obtained after converting the intensity produced by the transducer coupled to the thermocouple was used as the temperature reference. The data are listed in Table A.1.

The following conversions were carried out with these readings:

- Conversion of the binary readings of the converter directly to temperature: The full design range for the standard (4–20 mA) was used for this purpose, together with the maximum count of the 16-bit A/D converter (65,536). The results are present in the column labeled: "Temp. ref. (°C)".

Table A.1: Readings obtained prior to data treatment.

| Temp. on the soldering iron display (°C) | Current (mA) | Binary readings | Reference temp. (°C) |
|---|---|---|---|
| Off | 4.53 | 14868 | 19.875 |
| 100 | 7.89 | 21529 | 145.875 |
| 150 | 8.53 | 22854 | 169.875 |
| 200 | 9.89 | 25518 | 220.875 |
| 250 | 10.63 | 27014 | 248.625 |
| 300 | 11.27 | 28271 | 272.625 |
| 350 | 12.51 | 30738 | 319.125 |
| 400 | 12.86 | 31464 | 332.25 |
| 450 | 13.76 | 33200 | 366 |

The average error in the intensity reading (actual reading versus reading obtained with the multimeter) has been subtracted from the results of each current measurement. The results are presented in the column labeled "Corrected converter measurements (mA)". With this corrected current value, the conversion is made to degrees Celsius, using the start and full scale, both for temperature and intensity, provided by the manufacturer of the thermocouple-transducer (4–20 mA and 0-600 °C).

Table A.2: Corrections for current readings using the full binary and current ranges.

| **Current (mA)** | **Binary readings** | **Temp. ref.(°C)** | **A/D converter current (mA)** | **Multimeter vs. converter (mA)** | **Corrected converter measurements (mA)** | **Corrected temp. data (°C)** | **Reference vs. temp. corrected (°C)** |
|---|---|---|---|---|---|---|---|
| 4.53 | 14868 | 19.875 | 3.629882813 | 0.900117188 | 7.45050781 | 129.394043 | -109.519043 |
| 7.89 | 21529 | 145.875 | 5.256103516 | 2.633896484 | 9.07672852 | 190.3773193 | -44.50231934 |
| 8.53 | 22854 | 169.875 | 5.579589844 | 2.950410156 | 9.40021484 | 202.5080566 | -32.63305664 |
| 9.89 | 25518 | 220.875 | 6.229980469 | 3.660019531 | 10.0506055 | 226.8977051 | -6.022705078 |
| 10.63 | 27014 | 248.625 | 6.595214844 | 4.034785156 | 10.4158398 | 240.5939941 | 8.031005859 |
| 11.27 | 28271 | 272.625 | 6.902099609 | 4.367900391 | 10.7227246 | 252.1021729 | 20.52282715 |
| 12.51 | 30738 | 319.125 | 7.504394531 | 5.005605469 | 11.3250195 | 274.6882324 | 44.43676758 |
| 12.86 | 31464 | 332.25 | 7.681640625 | 5.178359375 | 11.5022656 | 281.3349609 | 50.91503906 |
| 13.76 | 33200 | 366 | 8.10546875 | 5.65453125 | 11.9260938 | 297.2285156 | 68.77148438 |
| | | | **Average error (mA)** | 3.820625 | | | |

The difference between the amperage and temperature readings with respect to the references was significant.

- Use of the maximum and minimum values obtained with the multimeter as a current refer-

ence: In this case, the maximum and minimum ranges obtained experimentally were used for the current and the converter readings, corresponding to the values mentioned in Appendix A (3.2–21.83 mA and 12,206–49,384 in binary). The results are shown in the column labeled "Calibrated current (mA)".

Adjustments were made by subtracting the average error obtained from each calibrated measurement to improve the reading process. Thus, a reading closer to the value obtained using the ammeter was obtained.

This final value, together with the ranges supplied by the manufacturer (4–20 mA and 0–600 °C), allows for the final conversion to determine the temperature for use in the experimental stage.

Table A.3: Corrections for current readings using the empirical binary and intensity ranges.

| Current (mA) | Binary readings | Temp. ref. (°C) | Calibrated current (mA) | Ref. vs. calibrated value (mA) | Corrected converter measurement (mA) | Corrected temperature data (°C) | Ref. vs. corrected value (°C) |
|---|---|---|---|---|---|---|---|
| 4.53 | 14868 | 19.875 | 7.45039647 | -2.920396471 | 4.54843408 | 20.566278 | -0.69 |
| 7.89 | 21529 | 145.875 | 10.7882422 | -2.89824224 | 7.88627985 | 145.7354943 | 0.14 |
| 8.53 | 22854 | 169.875 | 11.4522035 | -2.922203454 | 8.55024106 | 170.6340398 | -0.76 |
| 9.89 | 25518 | 220.875 | 12.7871413 | -2.89714132 | 9.88517893 | 220.6942098 | 0.18 |
| 10.63 | 27014 | 248.625 | 13.5367911 | -2.906791113 | 10.6348287 | 248.8060771 | -0.18 |
| 11.27 | 28271 | 272.625 | 14.1666773 | -2.896677336 | 11.2647149 | 272.4268104 | 0.20 |
| 12.51 | 30738 | 319.125 | 15.402898 | -2.89289795 | 12.5009356 | 318.7850835 | 0.34 |
| 12.86 | 31464 | 332.25 | 15.7666986 | -2.906698585 | 12.8647362 | 332.4276073 | -0.18 |
| 13.76 | 33200 | 366 | 16.6366131 | -2.876613051 | 13.7346507 | 365.0493997 | 0.95 |
| | | | average error (mA) | -2.901962391 | | | |

When presenting the data, the elevated temperature pyrolysis process does not require centesimal precision to reach the desired temperature of 800 °C (the objective is to maintain the set point temperature with a margin of ±25 °C) because the system, by its construction, has a high thermal inertia. Additionally, the maximum temperature to be reached depends on the material introduced into the system and the average humidity of the fuel, which varies throughout the combustion process.

Therefore, this adjustment process is considered good, taking into consideration the con-

struction characteristics, the fact that the adjusted measurements are remarkably close to the real values, and that the design prioritises portability and economic factors.

### *B.2. Flow rate calibration*

According to the simulations, the flow rate that could circulate through the system was 50 $m^3$/h. Therefore, a conjunction Venturi tube and a differential pressure gauge were designed to satisfy this requirement (the calculations that justify this statement are provided in Appendix B). For the calibration of the Venturi tube, a flow meter was used, which could measure up to 200 L/min (12 $m^3$/h) (SFM3000). The air flow is provided by an electric blower that delivers a fixed flow rate of 2.3 $m^3$/min (138 $m^3$/h).

However, the assembly has two limitations:

1. The flow rate provided by the blower is higher than of the setup with the Venturi and digital flow meters.
2. The flowmeter does not reach the maximum design range.

Therefore, we decided to install a flow divider or Y-valve. This system has two regulators to control the opening of each division, as shown in Fig. C.2.

Because the flow provided by the blower was superior to the measurement capacity of the flow meter used as a reference, we decided to open the regulator that expels the injected air to the outside as much as possible. Another regulator was used to control the inlet flow to the measuring devices from full closure to full opening.

Because of the internal operation of the Y-valve, a part of the inlet air flow is lost; therefore, once the inlet regulator towards the measuring elements is completely open, the outlet regulator is closed until it reaches the maximum of the reference flowmeter.

Next, we discuss the development of the Venturi tube adjustment process using the SFM3000 flowmeter. The results obtained using both procedures were compared, and the necessary adjustments were made to obtain the best possible measurement.

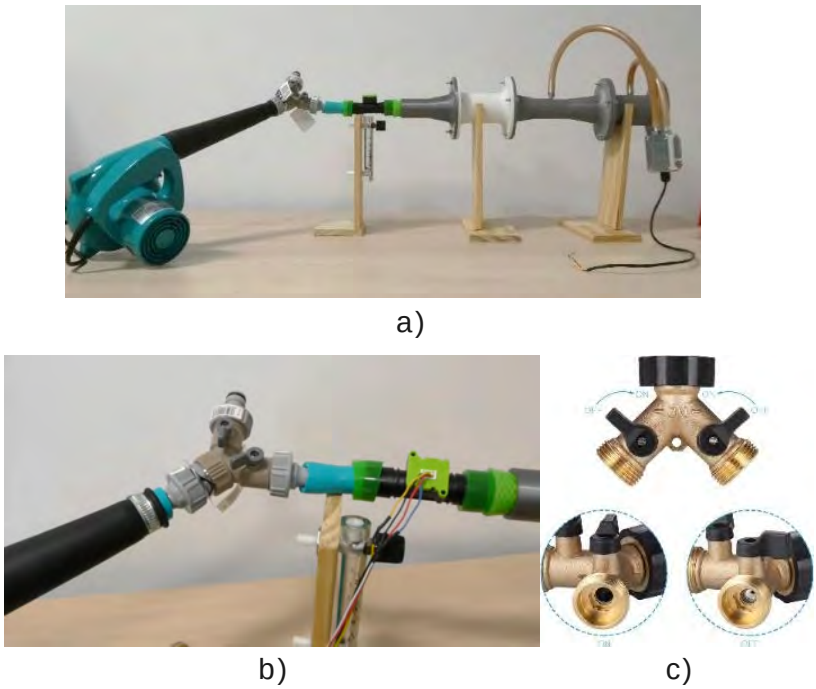


Figure C.2: a) Complete assembly for flow measurement and calibration. b) Details of the flow divider and reference flow meter. c) Y-valve operation.

Prior to the measurement stage, the operation of the different sensors was tested without any flow or saturation by the direct injection of the flow provided by the blower. The values listed in A.4 were obtained from this preliminary experiment.

Table A.4: Empirical measuring range of the different flow sensors together with the A/D converter.

| | **Start of range** | **End of range** |
|---|---|---|
| A/D converted (mA) | 3.2 | 21.83 |
| Binary readings | 12206 | 49384 |
| Pressure sensor | 0 | 500 |
| $p$ (mA) | 4.19 | 21.26 |
| $p$ (bin) | 1412 | 48226 |
| SFM3000 (16bits) | 32000 | 62800 |
| SFM3000 (14bits) | 8000 | 15700 |
| SFM3000 (l/min) | 0 | 200 |

The SFM3000 flow meter has a resolution of 14 bits, but the data provided by the A/D converter are 16 bits; therefore, the result of the 16-bit measurement was divided by 4. Thus, the

816 measurement range is adjusted according to the device resolution.

817 The measurement was conducted starting with the system without flow redirected to the mea-
818 surement equipment and then modifying the flow redirection in 0.05 mA jumps between mea-
819 surements. Following this process, 4.21 mA was obtained without a flow, and, by the end of the
820 SFM3000 measurement range, approximately 4.68 mA was recorded. The data obtained by the
821 flow meter composed of the Venturi tube and differential pressure meter are listed in Table A.5,
822 and those of the flow meter taken as reference in Table A.6.

Table A.5: Measurements obtained with Venturi assembly.

| Analog input number | Current (mA) | Binary readings |
|---|---|---|
| 6 | 4.21 | 14227 |
| | 4.25 | 14318 |
| | 4.30 | 14404 |
| | 4.35 | 14528 |
| | 4.40 | 14609 |
| | 4.45 | 14735 |
| | 4.50 | 14923 |
| | 4.55 | 14932 |
| | 4.60 | 14963 |
| | 4.68 | 15284 |

823 As the data provided by both sensors do not use the same scale or unit, it will be necessary
824 to perform a series of transformations. However, before comparing converted results from both
825 sensors, adjustments were made to the measurements by considering the starting and full-scale
826 values discussed above (Table A.4).

827 Regarding the conversion and adjustment of the data for the differential pressure sensor, this
828 sensor uses the 4–20 mA standard; therefore, the measurements obtained from the A/D converter
829 should be modified to be as close as possible to the value obtained by the multimeter. Four criteria
830 are applied, grouped as follows:

831 Considering the number of A/D converter bits: The converter has 16 bits; thus, for the mea-

Table A.6: Measurements obtained with the SFM3000 flowmeter, together with the intensity supplied with the differential pressure meter.

| Analog input number | Current (mA) | SFM3000 16bits | SFM3000 14bits |
|---|---|---|---|
| 5 | 4.21 | 32020 | 8005 |
| | 4.25 | 42420 | 10605 |
| | 4.3 | 48716 | 12179 |
| | 4.35 | 51288 | 12822 |
| | 4.4 | 54272 | 13568 |
| | 4.45 | 58012 | 14503 |
| | 4.5 | 58556 | 14639 |
| | 4.55 | 58916 | 14729 |
| | 4.6 | 59972 | 14993 |
| | 4.68 | 62790 | 15698 |

surement range of 4–20 mA, up to 65,536 combinations can be obtained. The results obtained using this criterion are shown in the column labeled “Full range current (mA)”. With this option, an average error of 0.84 mA was obtained with respect to the measurement obtained with the laboratory multimeter. The results obtained by subtracting the average error from the converted reading are presented in the column labeled “Corrected full range (mA)”.

Considering the measurements made with the multimeter, taking into consideration the start and full scale of the differential pressure sensor (4.19–21.26 mA) and their respective representations in binary (1412 and 48,226): When using the empirically obtained values, errors due to the tolerance of the passive elements and accessory circuitry connected to the A/D converter are considered. The data obtained from this transformation are presented in the column labeled “Full range corrected (mA)”. Consequently, an average error of 0.928319627 mA was obtained with respect to the measurement provided by the TTi multimeter. The results obtained by subtracting the average error from the converted reading are displayed in the column named “Corrected Value (mA)”.

This last method obtains the results closest to the value obtained by the laboratory multimeter; therefore, it is used for conversion from pressure to flow rate. The corrected current is then

Table A.7: Calibration of A/D converter current reading.

| Current (mA) | Binary readings | Full range current (mA) | Reference vs. full range (mA) | Corrected full range (mA) | Corrected converter measurements (mA) | Reference vs. sensor (mA) | Corrected value (mA) |
|---|---|---|---|---|---|---|---|
| 4.21 | 14227 | 3.473388672 | -0.736611328 | 4.32 | 5.187655189 | 0.977655189 | 4.26 |
| 4.25 | 14318 | 3.495605469 | -0.754394531 | 4.34 | 5.220836929 | 0.970836929 | 4.29 |
| 4.3 | 14404 | 3.516601563 | -0.783398438 | 4.36 | 5.252195497 | 0.952195497 | 4.32 |
| 4.35 | 14528 | 3.546875 | -0.803125 | 4.39 | 5.297410176 | 0.947410176 | 4.37 |
| 4.4 | 14609 | 3.566650391 | -0.833349609 | 4.41 | 5.326945572 | 0.926945572 | 4.40 |
| 4.45 | 14735 | 3.597412109 | -0.852587891 | 4.44 | 5.37288952 | 0.92288952 | 4.44 |
| 4.5 | 14923 | 3.643310547 | -0.856689453 | 4.49 | 5.441440808 | 0.941440808 | 4.51 |
| 4.55 | 14932 | 3.645507813 | -0.904492188 | 4.49 | 5.444722519 | 0.894722519 | 4.52 |
| 4.6 | 14963 | 3.653076172 | -0.946923828 | 4.50 | 5.456026189 | 0.856026189 | 4.53 |
| 4.68 | 15284 | 3.731445313 | -0.948554688 | 4.57 | 5.573073867 | 0.893073867 | 4.64 |
| | | **Average error (mA)** | -0.842012695 | | **Average error (mA)** | 0.928319627 | |

converted into pressure (Pa).

To obtain the conversion, the corrected current value (minus the start of the range, 4.19 mA) was multiplied by the end of the pressure range that the differential pressure meter could measure (500 to 0 Pa). This result is divided by the difference in measured current between the start and end of the measurement range (21.26–4.19 mA) to obtain the pressure in pascals (Pa).

Finally, to convert this pressure measurement to the flow rate, Eq. (B.9) was used (see Appendix B). By extracting all the constant terms from the proposed Venturi tube, a constant value equal to $9.76465 \cdot 10^{-4}$ was obtained. The relationship between the pressure drop due to the change in the section and the flow rate through the tube is shown in Eq. (C.1).

$$Q = A_1 A_2 \sqrt{\frac{2\,|\Delta p|}{\rho\,|A_2^2 - A_1^2|}} \tag{C.1}$$

If the square root of the result in Pascals is multiplied by this constant, the result in $m^3/s$ is obtained. To convert the value to $m^3/h$, we only need to multiply it by 3600. The correlations of the steps discussed in the previous two paragraphs, the correlations in Table 10 are obtained.

As a result of the steps discussed in the previous two paragraphs, the correlations in Table A.8 are obtained.

Regarding the conversion and adjustment of the data obtained by the flowmeter, the device used

Table A.8: Venturi pressure and flow measurements.

| $p$ (Pa) corrected value | $Q$ ($m^3$/h) corrected value |
|---|---|
| 2.03091863 | 5.00962747 |
| 3.002850103 | 6.091524521 |
| 3.921378748 | 6.961111104 |
| 5.245768888 | 8.051258053 |
| 6.110894705 | 8.689835801 |
| 7.456645976 | 9.599109198 |
| 9.464592317 | 10.81459166 |
| 9.560717408 | 10.86937096 |
| 9.891814943 | 11.05597789 |
| 13.32027651 | 12.82967899 |

as a reference to measure the airflow rate for laboratory calibration is the SENSIRION SFM3000 (Fig. C.3). It can measure up to 200 NL/min with a resolution of 14 bits, and its information is transmitted through the $I^2C$ communications protocol. It is designed for use with gases such as air, oxygen, and other nonaggressive gases, creating an extremely low pressure drop in the measurement. This makes it particularly interesting for use in medical applications, environmental monitoring, and laboratories.


Figure C.3: SENSIRION SFM3000 flowmeter.

For using this measuring device with the control system, 14-bit readings must be placed in a 16-bit variable, occupying the 14 most significant bits, with the two least significant bits always

being zero. Thus, the measurements obtained must be divided by 4 to obtain the correct result. Before connecting the flow meter to the Venturi tube and calibrating both measurement systems, measurements were obtained from the system with no load and under saturated conditions, and the results are listed in Table A.9.

Table A.9: Empirically obtained extremes with flow sensor.

| Condition | Flow (l/min) | 16-bits readings | 14-bits readings |
|---|---|---|---|
| Without any flow | 0 | 32000 | 8000 |
| Saturated | 200 | 62800 | 15700 |

To adjust the measurements, two methods were proposed, the results of which are listed in Table A.10:

1. Using the ranges provided by the manufacturer (0-16,834 binary for 0-200 L/min). The results for this method are shown in the column labeled "Default scaled flow (L/min)" and, after changing the units, in the column labeled "Default scaled flow ($m^3$/h)".

2. Use the empirically obtained extremes (Table A.9). The corresponding results are shown in the columns "Flow with calibrated scale" in L/min $m^3$/h, respectively.

Table A.10: Flow measurements obtained with the SFM3000 flowmeter.

| 14-bits readings | Default scaled flow (l/min) | Default scaled flow ($m^3$/h) | Flow with calibrated scale (l/min) | Flow with calibrated scale ($m^3$/h) |
|---|---|---|---|---|
| 8005 | 0.119274809 | 0.007156489 | 0.12987013 | 0.007792208 |
| 10605 | 129.4555664 | 7.767333984 | 67.66233766 | 4.05974026 |
| 12179 | 148.6694336 | 8.920166016 | 108.5454545 | 6.512727273 |
| 12822 | 156.5185547 | 9.391113281 | 125.2467532 | 7.514805195 |
| 13568 | 165.625 | 9.9375 | 144.6233766 | 8.677402597 |
| 14503 | 177.0385742 | 10.62231445 | 168.9090909 | 10.13454545 |
| 14639 | 178.6987305 | 10.72192383 | 172.4415584 | 10.34649351 |
| 14729 | 179.7973633 | 10.7878418 | 174.7792208 | 10.48675325 |
| 14993 | 183.0200195 | 10.98120117 | 181.6363636 | 10.89818182 |
| 15698 | 191.619873 | 11.49719238 | 199.9350649 | 11.9961039 |

The most interesting results were obtained using the calibration measurements.

Finally, the results and corrections of the Venturi tube setup were compared. From the results mentioned above, the outputs of both flow measurement systems can be compared.

Once the comparison between both columns was made, the same procedure described above was applied: subtracting the average error, obtained as the difference between the value used as the reference and that of the sensor to be corrected, from the flow meter composed of the union of the Venturi tube and the differential pressure sensor. The results are presented in Table A.11:

Table A.11: Comparison of flow rates obtained between the SFM3000 sensor and the Venturi plus differential pressure sensor.

| SFM3000 flow rate ($m^3/h$) | Flow rate measured by the Venturi ($m^3/h$) | SFM3000 vs. Venturi ($m^3/h$) | Corrected Venturi flow readings ($m^3/h$) |
|---|---|---|---|
| 0.007792208 | 5.00962747 | -5.001835262 | 4.08 |
| 4.05974026 | 6.091524521 | -2.031784262 | 5.16 |
| 6.512727273 | 6.961111104 | -0.448383832 | 6.03 |
| 7.514805195 | 8.051258053 | -0.536452858 | 7.12 |
| 8.677402597 | 8.689835801 | -0.012433204 | 7.76 |
| 10.13454545 | 9.599109198 | 0.535436256 | 8.67 |
| 10.34649351 | 10.81459166 | -0.468098153 | 9.88 |
| 10.48675325 | 10.86937096 | -0.382617709 | 9.94 |
| 10.89818182 | 11.05597789 | -0.157796071 | 10.12 |
| 11.9961039 | 12.82967899 | -0.833575098 | 11.90 |
| | **Average error ($m^3/h$)** | 0.93 | |

Therefore, it can be concluded that, with the correction, the flow rate measured by the differential pressure sensor is sufficiently accurate for use in the prototype. However, complications must be considered when the reading flow rates are close to 0 $m^3/h$.